

# Robotic observations of high wintertime carbon export in California coastal waters

J. K. B. Bishop<sup>1,2</sup>, M. B. Fong<sup>3</sup>, T. J. Wood<sup>2</sup>

<sup>1</sup>Department of Earth and Planetary Science, UC Berkeley, Berkeley, CA 94720, USA.

<sup>2</sup>Earth Sciences Division, Lawrence Berkeley National Laboratory, Berkeley, CA, 94720, USA

5 <sup>3</sup>Department of Chemistry, Scripps Institution of Oceanography, La Jolla, CA, USA.

*Correspondence to:* J. K. B. Bishop (jkbishop@berkeley.edu)

## Abstract.

Biologically mediated particulate organic and inorganic carbon (POC and PIC) export from surface waters is the principal determinant of the vertical oceanic distribution of pH and dissolved inorganic carbon and thus sets the conditions for air sea exchange of CO<sub>2</sub>; exported organic matter also provides the energy fuelling communities in the mesopelagic zone. However, observations are temporally and spatially sparse. Here we report first hourly-resolved optically-quantified POC and PIC sedimentation rate time series from autonomous Lagrangian Carbon Flux Explorers (CFEs), which monitored particle flux using an imaging optical sedimentation recorder (OSR) at depths below 140 m in the Santa Cruz Basin, CA in May 2012, and in January and March 2013. Highest POC vertical flux (~100-240 mmol C m<sup>-2</sup> d<sup>-1</sup>) occurred in January, when most settling material was mm to cm-sized aggregates, but when surface biomass was low; fluxes were ~18 and ~6 mmol C m<sup>-2</sup> d<sup>-1</sup>, respectively in March and May, under high surface biomass conditions. An unexpected discovery was that January 2013 fluxes measured by CFE were 20 times higher than that measured by simultaneously deployed surface-tethered OSR; multiple lines of evidence indicate strong undersampling of aggregates larger than 1 mm in the later case. Furthermore, the Jan 2013 CFE fluxes were about 10 times higher than observed during multi year sediment trap observations in the nearby Santa Barbara and San Pedro Basins. The strength of carbon export in biologically dynamic California coastal waters is likely underestimated by at least a factor of 3 and at times by a factor of 20.

25 **Key words.** Biological Carbon Pump, Ocean Carbon Cycle, Twilight Zone Export, Coastal Sedimentation, Optical Sedimentation Recorder, Carbon Flux Explorer.

## 1. Introduction

Phytoplankton account for half of global net photosynthesis (Field et al., 1988), or about 50 Pg C y<sup>-1</sup>, yet they live for a week before being removed from the euphotic zone through grazing or abiotic aggregation processes. While most phytoplankton carbon is recycled in the surface layer, recent model and observation based estimates (Henson *et al.*, 2011; Yao and Schlitzer 2013; Siegel *et al.*, 2014) suggest that globally 5 to 12 Pg C y<sup>-1</sup> is exported below the euphotic zone as sinking particulate organic and inorganic carbon (POC and PIC) in fecal pellets, amorphous large aggregates, and as independently sinking carapaces and calcareous shells (e.g. Bishop, Ketten, and Edmond, 1978; Alldredge and Silver 1988; Turner, 2015). Many large amorphous aggregate particles (e.g. greater in size than 0.5

mm) would also be classified as marine snow by virtue of their being visible to the naked eye or camera in reflected light; such aggregates have been shown to originate as products of feeding (e.g. ejected boluses of fecal material, or discarded mucus feeding webs, or appendicularian houses) or from turbulence driven aggregation of biogenic organic and inorganic particles (Aldredge and Silver 1988). Important to POC settling is particulate inorganic carbon (i.e. PIC), in the form of calcite foraminifera shells and coccolith plates and aragonite pteropod shells and shell fragments. Foraminifera shells preserved in sediments in particular are key to unravelling past climate and ocean chemistry, yet little of their dynamics in the water column has been understood (e.g. Be *et al.*, 1985). Together with siliceous diatom frustules and radiolarian tests, biogenic carbonates are a major factor governing the excess density, and hence sinking rate, of aggregate particles carrying POC downward from the surface layer (Armstrong *et al.*, 2002). As much of exported organic matter is consumed in the water column or at the sediment sea water interface, little POC is preserved in sediments. The varied processes of production, grazing, recycling, export, and subsurface remineralisation constitute the ocean's biological carbon pump (Volk and Hoffert, 1985).

Direct observations of POC and PIC sedimentation fluxes in the upper thousand meters of the ocean are sparse, of short duration (days), and with few exceptions, are mostly during summertime. This is because all observations to date have required ships to be present or nearby (e.g. Martin *et al.*, 1987; Buesseler *et al.*, 2000; Stanley *et al.*, 2004; Lam and Bishop, 2007; Lampitt *et al.*, 2008; Lee *et al.*, 2009; Owens *et al.*, 2013).

Such direct observations are often used to calibrate models used to estimate global carbon export (e.g. Henson *et al.*, 2011, Siegel *et al.*, 2014). Henson *et al.* (2011) estimated an export of 5 Pg C y<sup>-1</sup>, based on the synthesis of a decade of ship observations of the ratio of dissolved radioactive <sup>234</sup>Th to parent <sup>238</sup>U, <sup>234</sup>Th/POC ratios measured in shallow sediment trap or pump sampled particulates, and satellite-based estimates of primary productivity. Siegel *et al.* (2014) estimated a global carbon export of 6 Pg C y<sup>-1</sup> using the combination of food web models – calibrated with ship-board observations of production, grazing, and sedimentation -- and global satellite retrievals of size-dependent phytoplankton biomass. In contrast, Yao and Schlitzer (2013) estimated an export of 12 Pg C y<sup>-1</sup> by inversion, within an ocean circulation model, of ocean nutrient fields averaged over five to six decades. It is unknown whether the factor of two difference in export numbers are a reflection of a strong, recent weakening biological carbon pump, or of differences in methodology. Either way, there is major uncertainty in both the strength and stability of the ocean's biological carbon pump and of consequent feedbacks to atmospheric CO<sub>2</sub> trends; furthermore, there remains major uncertainty as to the magnitude of the energy flow carried by sinking particles to sustain mesopelagic communities (Burd, *et al.* 2010; Banse, 2013).

Eppley and Peterson (1979; E&P) pointed out the importance of near-shore waters, defined as coastal waters deeper than 200 m, to the ocean carbon cycle. In their estimate, near-shore waters account for over 40% of global new production and hence particle export. While there have been arguments that this number may be somewhat high in the modern context (Henson *et al.*, 2011), all recent calculations of global export (although not broken down as done as in E&P 1979) indicate a lower contribution from coastal waters.

In this paper, we describe direct in-situ observations of carbon export in biologically dynamic ocean waters near the California coast obtained using a fully autonomous ocean profiling Carbon Flux Explorer (CFE; Fig. 1A) that we have developed. The Carbon Flux Explorer is designed to perform sustained high-frequency observations of POC

and PIC sedimentation within the upper kilometer (or twilight zone) of the ocean for seasons to years and to operate in an observational context not dependent on ships. The CFE melds the concept of current-following, sample-collecting neutrally-buoyant sediment traps (Buesseler *et al.*, 2000; Stanley *et al.*, 2004, Lampitt *et al.*, 2008, Owens *et al.*, 2013) with photographic imaging of the particles as they are deposited in a sediment trap (Asper, 1987). The  
5 current-following approach aims to avoid the hydrodynamic biases suffered by surface tethered sediment traps (Gardner, 2000; Buesseler *et al.*, 2007).

Bishop *et al.* (2004, 2009) and Estapa *et al.* (2013) have deployed transmissometer equipped profiling floats to observe the high-frequency variability of the systematics of sedimentation. When the floats yo-yo from depth to the surface, transmissometers record the concentration variability of particles in the water column. As the floats drift at  
10 depth between profiles, there is a measurable transmission loss (or attenuation increase) as settled particles accumulate on the upward looking transmissometer window. These data, when normalized by the time at depth, yield a simple metric, or index, of sedimentation. In contrast, with direct high-resolution imaging of the settled particles, the CFE not only is able to quantify optical metrics of particle flux, but also is able to gain detail on kinds of particles and thus the specifics of the process governing carbon export.

15 Below we present observations from CFE development testing during three expeditions off the coast of southern California aboard R/V New Horizon: May 29-June 4 2012 (NH1204), Jan. 18-21 2013 (NH1301) and March 27-31 2013 (NH1304). These observations, like past ship-tended studies using neutrally buoyant and surface-tethered sediment traps, are of relatively short duration (days); however, they are the first carried out in a productive coastal environment. CFE data are analysed below in the framework of remotely sensed surface chlorophyll and POC, *in-situ*  
20 water column optical properties, and subsurface currents. The study site is a 150 km<sup>2</sup> region centred at 33° 43'N 119° 33'W in the 1900 m deep Santa Cruz Basin (SCB) near the California coast (Figs. 1B & C).

## 2. Methods

### 2.1 Carbon Flux Explorer (CFE).

The CFE is comprised of an Optical Sedimentation Recorder (OSR) interfaced to a CTD-equipped Sounding  
25 Oceanographic Lagrangian Observer (SOLO) float (Davis, Sherman and Dufor, 2001). The CFE dives repeatedly (daily in this study) below the surface to obtain OSR observations at three target depths. The CFE's Optical Sedimentation Recorder (OSR; Figure A1, Appendix Sec. 1.1) awakes when the CFE reaches a target depth. Particles settle through a hexagonal celled baffle (1 cm opening, 5 cm length) into a high-aspect titanium funnel and settling column before depositing on a 2.54 cm diameter glass sample stage; funnel diameter is 15.4 cm. Particles are imaged  
30 in three lighting modes: transmitted, transmitted-cross-polarized, and dark field. On first wake up of a given dive, the sample stage is flushed with water and images of the particle-free stage are obtained. At timed intervals (~20 min in data described here) the OSR repeats image sets, which register the sequential build-up of particles. After the pre-determined number of image sets over ~1.8 hours, cleaning occurs and a new reference image set is obtained. After  
~5 hours at a target depth the OSR performs a final image/cleaning cycle and reference image set, and the SOLO  
35 surfaces to report GPS position, CTD profile data, and OSR engineering data, and dives to its next target depth.

Every 3 dive cycles, the depth order is repeated; in the current study, target depths were 150, 300 and 500m. A ballasting error in May 2012 led to the CFE operating 300 to 400m deeper than planned. In the CFE described here, all images were stored aboard the OSR for post recovery analysis.

## **2.2 OSR Image data reduction.**

5 Images were taken under transmitted, transmitted-cross-polarized, and dark field illumination, and were processed to yield three parameters that characterize particle abundance, according to the scheme depicted in Fig. 2. The parameters are particle attenuation, cross-polarized photon yield, and dark field counts. Attenuance is the best measure of particle loading as light is reduced exponentially as it propagates through the sample. Cross-polarized photon yield takes advantage of the birefringent property of calcium carbonate, and is a measure of particulate  
10 inorganic carbon. Dark field counts reveal the colour of particles. Details of the treatment of transmitted light and transmitted cross-polarized light images are covered in sections 2.2.1 and 2.2.2, respectively. Dark-field images are normalized by illumination intensity and then transformed to a consistently scaled reflectance in counts above background. A full-resolution post-processing image of an aggregate particle from January 2013 is shown for all modes of illumination in Figure 3.

### **15 2.2.1 Attenuance (ATN).**

Transmitted light (TRA) images are normalized by an in-situ particle free image of the sample stage area under transmitted light illumination. Image attenuation (ATN), the sum of both light scattering loss and particle absorption of the primary beam, is calculated as the negative  $\log_{10}$  of transmittance and is a measure of both aggregate thickness and transparency. The effects of overlaying particles are additive in attenuation units. We calculate attenuation in  $\log_{10}$   
20 units rather than in natural log units as order-of-magnitude changes of transmission are easy to infer. Attenuance data reported here may be converted to natural log units by multiplying by 2.303.

In order to detect particles, we set the lowest threshold of pixel attenuation to be 0.02. The attenuation of all pixels identified as particles is integrated across sample stage area and then divided by the total number of pixels of the sample stage area to yield the average particle load of the sample stage (in attenuation units). For convenience  
25 attenuation is multiplied by 1000 and reported in units of milli-attenuance (mATN). The stage load, when multiplied by sample stage area yields units of  $\text{mATN}\cdot\text{cm}^2$ . Because the light source is directly above the sample stage, the stage load ( $\text{mATN}\cdot\text{cm}^2$ ) is an optical ‘volume’ of material on the sample stage. Attenuance flux (in units of  $\text{mATN}\cdot\text{cm}^2\text{ cm}^{-2}\text{ d}^{-1}$ ) is calculated by taking differences of successive stage loads, divided by the mouth opening of the trap, and further divided by the time (in days) between image sets. Attenuance is never saturated in our images (e.g.  
30 transmission is always greater than 0).

### **2.2.2 Cross-Polarized Photon Yield (POL).**

Transmitted, cross-polarized light images are processed in three steps: compensation for the attenuation effects of particles, subtraction of the particle-free blank and normalization for light source intensity. Due to the isolation of sub-stage polarizer in the pressure case of the OSR, hydrostatically induced stress on the glass pressure case window

at depth induces an interference seen by the camera; thus, absorbing particles appear dark in the uncorrected image (Fig. 2B – RAW POL Image). The absorption effect is compensated by division of observed image counts by a polarization compensation factor (PCF), an empirically derived function of attenuation:  $PCF = 1/(2.1 * ATN)$ . This stress polarization interference has been eliminated in later builds of the CFE by moving the sub-stage polarizer  
5 outside of the pressure case.

Following correction, image counts at each pixel (for particles identified using the 0.02 attenuation threshold) are integrated across all particle pixels and normalized by the total number of pixels covering the stage area. Sample counts are normalized to lamp brightness and scaled by the difference in exposure time for POL vs. TRA images to yield the quantity cross-polarized photon yield, expressed as a fraction of incident beam intensity. Results are scaled  
10 up by  $10^6$  and data are reported in ppm. This optical measure of flux is in units of  $\text{ppm-cm}^2 \text{ cm}^{-2} \text{ d}^{-1}$ .

### 2.2.3 Interference by Swimmers.

In the PIC flux time series, there were several instances when a calcified swimming organism was detected. This mainly affected data from expedition NH1304, and Cyprid barnacle larvae were the predominant interfering organism. When the appearance and disappearance of these organisms in the image series led to a strong positive  
15 then negative flux, the interfering flux estimate was eliminated from the 1.8 hour average. In one other case during NH1304, a calcified amphipod carapace (Fig. 4-B) was removed from the 1.8 hour average PIC flux. This carapace was clearly part of the flux but was excluded in our consideration of aggregate sedimentation. Excluded points in Fig. 5B (below) are indicated by circled (+) symbols. Attenuance flux data were not modified as swimmer interference did not alter the signal in a dominant way.

### 20 2.2.4 POC and PIC flux proxy.

We hypothesize that attenuation is the best proxy for the POC in particles by analogy to the finding that transmissometer measured particle beam attenuation coefficient ( $c_p$ ) is highly correlated to POC concentration (e.g., Bishop and Wood, 2008). We note that particle beam attenuation coefficient is expressed in units of  $\text{m}^{-1}$  while our attenuation values are dimensionless. This is because in transmissometry, beam attenuation occurs continuously along  
25 the seawater path that the light beam passes through. In our case, the path length from light to sample stage is unimportant as all attenuation of light occurs in the thin layer of particles on the sample stage. Our use of the image of the light source as a transmission reference removes the minor effects of light loss through the water path.

Cross-polarized photon yield is a measure of PIC, which is comprised of biogenic calcite and aragonite polymorphs of calcium carbonate. The photon yield under cross-polarized illumination (or birefringence) of carbonates has been  
30 shown to scale linearly with PIC concentration; furthermore, biogenic carbonates both dominate all mineral material in the water column and have 10 times greater photon yield compared with other birefringent minerals (Guay and Bishop, 2002).

### 2.3 Conversion of POC<sub>ATN</sub> flux to POC flux.

Calibration samples from the BUOY-OSR system were not useful due to a 20-fold lower particle collection rate compared to that of the CFE (described below in Sec. 3.3). We thus estimate the amount of POC in our images in order to translate attenuation flux to POC flux.

- 5 Bishop et al. (1978) report information on the dry weight density and geometric properties of particles of similar morphology as sampled here. Particularly, we use particle dry weight density of  $0.087 \text{ g cm}^{-3}$ , and the Bishop et al. (1978) equation, which estimates aggregate thickness (h, in cm) as a function of equivalent circular diameter (d, in cm):

$$h = 0.052d + 0.0045. \quad (1)$$

- We analysed a series of 5 images collected on January 20 2013 from 11:11:47 to 12:39:47 UTC (just before cleaning). The last  
10 image of this set had 65% of the sample stage covered with particles. These images are provided in supplemental material for readers to independently analyse. The software package ImageJ (National Institutes of Health, USA – <http://rsb.info.nih.gov/ij>) was used to measure the equivalent circular diameter of aggregates. As aggregates overlapped in successive images due to the unexpectedly high sedimentation observed, successive images were stepwise subtracted in pairs prior to size analysis. Aggregate volume was calculated as the product of cross sectional area and h.

- 15 A total of 127 aggregates from  $500 \mu\text{m}$  to  $8.3 \text{ mm}$  in size were enumerated in all five images. A size cutoff of  $800 \mu\text{m}$  was used to minimize contamination of the analysis due to the slight expansion of aggregate dimension over time as they rested on the stage. Although, size distributions were initially quantified to a lower limit of  $20 \mu\text{m}$ , it is important to note that 97% of the volume attenuation of the sample was accounted for by particles  $>800 \mu\text{m}$  in this sample. For the remaining 63 particles larger than  $800 \mu\text{m}$ , we calculated an aggregate volume of  $0.113 \text{ cm}^3$ . To estimate the POC flux, we assume an aggregate dry weight  
20 density of  $0.087 \text{ g cm}^3$  (e.g. From Fig. 22 in Bishop et al. 1978) and thus calculate the weight of aggregate matter as  $0.0098 \text{ g}$ . Organic matter at depths between  $100 \text{ m}$  and  $500 \text{ m}$  is typically 60% (range 50-70%) of dry weight (Fig. 11 in Bishop et al. 1978). Thus, organic matter weight is  $0.0059 \text{ g}$ . We estimate POC (as carbon) by dividing this mass by the OM:C conversion factor, 1.88 from Hedges et al. (2002). We divide by 12.011, the atomic weight of carbon, to yield a POC loading of  $0.26 \times 10^{-3}$  moles. The opening of the OSR funnel has a diameter of  $15.4 \text{ cm}$ , which yields an assumed trap collection area of  $186.3 \text{ cm}^2$ .  
25 The time interval for collection of this sample was 1.84 hours, or 0.0766 days. Combining this information yields a carbon flux of  $183 \text{ mmol m}^{-2} \text{ d}^{-1}$ . The average POC<sub>ATN</sub> flux for all particles  $>13 \mu\text{m}$  in size during the same time interval was  $66.2 \text{ mATN-cm}^2 \text{ cm}^{-2} \text{ d}^{-1}$ . As mentioned above, over 97% of cumulative sample attenuation was in the  $>800 \mu\text{m}$  size fraction. The conversion factor for POC<sub>ATN</sub> flux to POC flux is the ratio of 183 to  $66.2 \times 0.97 = 2.8$ . This conversion factor allows estimation of POC fluxes observed for compare with other data from near by waters.

- 30 Alldredge (1998) collected marine snow by scuba at euphotic depths of 10 to 20 m in the nearby Santa Barbara Basin. They imaged particles in the laboratory and derived maximum and minimum dimensions, and assumed an elliptical volume. From this they calculated equivalent spherical volume (ESV in  $\text{mm}^3$ ). Samples were analyzed for POC and a regression formula was derived ( $\text{POC} (\mu\text{g}) = 0.99 \times \text{ESV}^{0.52}$ ). If we use the ImageJ 2-dimensional analyses of minimum and maximum aggregate dimensions in our images to compute equivalent spherical volume (ESV) following Alldredge's methods we get ESV values that  
35 are 8.5 times higher than obtained using our approach. If we use the Alldredge (1988) conversion of ESV to POC/aggregate and sum over all particles  $>1 \text{ mm}$  in size, then the amount of POC is 17 times lower than our estimate. The Alldredge method yields a POC density for aggregates equal to  $0.00020 \text{ g C cm}^{-3}$  while our method yields  $\sim 0.028 \text{ g C cm}^{-3}$ . The carbon density of aggregate particles derived from their equations differs from ours by a factor of 140. We are not sure if there is a unit error in Alldredge (1998), or if the marine snow particles sampled in shallow waters were mostly empty of material, or if they deflate as

they sink below the euphotic zone. Bishop et al. (1978) describe aggregates sampled from 100-400 m that appeared similarly loaded to those described here; for this reason believe that our method is internally most consistent.

We stress that the factor 2.8, used for conversion of  $POC_{ATN}$  flux to POC flux is approximate. Equation (1) for aggregate thickness is the only applicable published study that we are aware of. The dry weight density factor ( $0.087 \text{ g cm}^{-3}$ ) was taken for aggregates that were similarly optically dense as observed in this sample. Bishop et al. (1978) also reported dry density values as high as  $0.24 \text{ g cm}^{-3}$ . The organic matter percentage for large particulates used in the calculation above is typical of values obtained by our group using in-situ filtration. We note that Collins et al. (2011) report upper water column POC flux and mass flux data from surface tethered sediment traps in the San Pedro Basin (Fig. 1), closer to shore, which yield values closer to 30% with the rest being contributed by inorganic terrigenous and biogenic phases. This would require our estimate of dry weight particle density to be proportionately adjusted upwards to account for the greater fraction of inorganic ballasting material – and thus compensate for the reduced organic percentage. A factor of two adjustment of the  $POC:POC_{ATN}$  ratio either way will not change our conclusions regarding the high magnitude of the sedimentation rate observed in January 2013 by the CFE. Nor will it change the relative difference observed between CFE and BUOY-OSR presented below.

## 2.4 Satellite data processing.

Retrievals of chlorophyll and POC from observations made by the Moderate-Resolution Imaging Spectroradiometer (MODIS) on NASA's Aqua satellite are provided on the NASA DAAC. Level 2 Local Area Coverage (L2-LAC) data at 1 km resolution for the period of the three expeditions were downloaded on April 4 2013 and processed using SEADAS software. Chlorophyll and POC were retrieved for pixels within a 2 km search radius of  $33.72^{\circ}\text{N}$   $119.5^{\circ}\text{W}$  and were selected using the standard ocean colour processing quality flags. Means and standard deviations were calculated and data were further selected based on the requirement of 5 valid pixels. Further analysis of spatial and temporal trends of chlorophyll within our study area is presented in Appendix section 1.3.

Surface photosynthetically active radiation (PAR) estimated from MODIS Aqua data for Jan., Mar., and May expeditions was 25, 45, and 60 Einsteins  $\text{m}^{-2} \text{d}^{-1}$ , respectively. Corresponding values for diffuse attenuation coefficient for PAR ( $k_{PAR}$ ) from beam attenuation coefficient profiles (Bishop and Wood, 2009) were 0.068, 0.20, and  $0.18 \text{ m}^{-1}$ . Euphotic zone depths corresponding to the 1% light level were 68, 23, and 26 m. The euphotic zone depths based on the  $1 \text{ E m}^{-2} \text{d}^{-1}$  isolume were 50, 20, and 25 m.

## 3. Results

### 3.1 Flux time-series, Hydrography, and Remote sensing data

Figure 5 shows the time series of  $POC_{ATN}$  flux and  $PIC_{POL}$  flux. In contrast to surface-tethered sediment traps (Martin et al., 1987), we found that the influence by/presence of swimming organisms was rarely significant in our image time series (see supplemental animations of CFE imagery). The highest  $POC_{ATN}$  flux was measured in Jan. 2013, intermediate flux was observed in March 2013, and lowest flux was observed in May 2012. Similar temporal/depth systematics was observed for  $PIC_{POL}$  flux (Fig. 5B); however, the relative ratio of  $PIC/POC$  flux was highest in March 2013.

The hydrographic context for our observations was established by CTD/transmissometer casts made to full water depth 3-4 times per day during each expedition. We found that mixed layer depths were mostly shallower than 10 m during all expeditions, reflective of the California coastal upwelling regime and net divergence of surface waters in the Santa Cruz Basin. We calculate properties of the upper 20 m, as these are most closely comparable to remotely sensed surface properties. Upper 20 m temperatures for January, March, and May averaged 12.6, 13.5, and 15 °C, respectively, reflecting seasonal warming. Over each cruise, averaged 0-20 m POC concentrations derived from transmissometer profiles ( $\pm$  s.d; Appendix A, Sec. 1.2 Fig. A2) were  $4.1 \pm 0.7$  (Jan.),  $17.5 \pm 3.4$  (March),  $15.4 \pm 5.7$   $\mu$ M (May). POC was most variable in May 2012, with concentrations rising from  $\sim 10$   $\mu$ M to 25  $\mu$ M over the period of observations reflecting the progression of a plankton bloom southward from Point Conception. Corresponding euphotic zone depths (EZD) based on the 1 Einstein  $\text{m}^{-2} \text{d}^{-1}$  isolume (EZD for 1% light level in parentheses) were 50 (68), 20 (23), and 25 (26) m, respectively. January and March 2013 showed little temporal POC trend indicating a quasi steady state balance of photosynthesis and loss processes (Appendix A, Sec 1.2 Fig. A2).

Figure 6 shows MODIS Aqua Chlorophyll and POC time series, averaged MODIS Chlorophyll and POC values for each cruise period and the previous week, averaged upper 20 m POC from CTD casts, and depth profiles of  $\text{POC}_{\text{ATN}}$  and  $\text{PIC}_{\text{POL}}$  flux. Satellite retrieved POC values agreed well with transmissometer estimates for March and May, and were lowest in January 2013, albeit approximately 2.5 times higher than transmissometer estimates. Imagery of the area in January the week prior to our cruise showed patchy (rather than organized) structure in chlorophyll distribution. During the time of the expedition, distributions were nearly spatially invariant on the scale of the study area (Supplemental materials, Appendix 1.3, Fig. A3). From all perspectives, January 2013 had the lowest phytoplankton biomass but by far the highest fluxes of POC and PIC.

### 3.2 Particle Flux Profiles

Averaged  $\text{POC}_{\text{ATN}}$  and  $\text{PIC}_{\text{POL}}$  flux profiles provide systematic quantification of depth trends of sedimentation. In Jan. 2013,  $\text{POC}_{\text{ATN}}$  fluxes at depths 150, 300 and 500 m were 67, 85, and 35  $\text{mATN-cm}^2 \text{cm}^{-2} \text{d}^{-1}$ , respectively; in Mar. 2013 at similar depths, flux was between 6 to 7  $\text{mATN-cm}^2 \text{cm}^{-2} \text{d}^{-1}$ ; values in May 2012 for the 450 – 900 m interval fell between 2 and 3  $\text{mATN-cm}^2 \text{cm}^{-2} \text{d}^{-1}$  with no depth trend.  $\text{PIC}_{\text{POL}}$  flux trends roughly followed those for  $\text{POC}_{\text{ATN}}$  flux.  $\text{PIC}_{\text{POL}}$  fluxes and at 150, 300 and 500 m depths were 96, 122, and 63  $\text{ppm-cm}^2 \text{cm}^{-2} \text{d}^{-1}$  (Jan. 2013) and 33, 15, and 16  $\text{ppm-cm}^2 \text{cm}^{-2} \text{d}^{-1}$  (Mar. 2013); The apparent decrease of PIC flux with depth from 2.8 to 0.5  $\text{ppm-cm}^2 \text{cm}^{-2} \text{d}^{-1}$  in May 2012 may be a consequence of the low flux condition and high scatter of points.

For both  $\text{POC}_{\text{ATN}}$  and  $\text{PIC}_{\text{POL}}$  flux, it is also notable that the 1.8 hour averaged fluxes for each depth ranged over a factor of 10 relative to their average for the May and March periods, but ranged by less than a factor of two in the high flux period January 2013. This suggests that sedimentation is more uniform when large aggregates dominate.

The profile of  $\text{PIC}_{\text{POL}}/\text{POC}_{\text{ATN}}$  ratio (Fig. 7) shows a depth dependent increase from 1.4 to 2.4 in January, indicating preferential loss of POC with sinking. In March,  $\text{PIC}_{\text{POL}}/\text{POC}_{\text{ATN}}$  ratios slightly decreased with depth from 4.6 to 3.7. In May 2012, PIC/POC ratio decreased from 1.5 to 0.3 between 430 and 900 m. The fact that the PIC/POC can decrease with depth suggests preferential carbonate dissolution can and does occur in shallow waters, a finding

consistent with Bishop and Wood (2008). These observations confirm that the relative contribution of carbonates to aggregate ballasting varies with time.

### 3.3 Comparison of Surface Tethered Optical Sedimentation Recorder (OSR) flux with CFE Flux

In January 2013, an OSR system, identical to the OSR on the CFE, was deployed at 237 m tethered below a buoy system at the surface (Appendix, Section 1.4, Fig. A4). This BUOY-OSR system was engineered to collect samples needed to calibrate the  $POC_{ATN}$  and  $PIC_{POL}$  data; however, this approach was a failure. The  $POC_{ATN}$  time series from CFE and BUOY-OSR are compared in Figure 8. The BUOY-OSR yielded  $POC_{ATN}$  and  $PIC_{ATN}$  fluxes of  $3.6 \text{ mATN-cm}^2 \text{ cm}^{-2} \text{ d}^{-1}$  and  $2.2 \text{ ppm-cm}^2 \text{ cm}^{-2} \text{ d}^{-1}$ , respectively – approximately 25 fold and 50 fold lower than CFE fluxes at 144 and 320 m depths. At the same time, BUOY-OSR and CFE images showed that the two systems collected aggregates of completely different morphology and size distribution (Fig. 9). The CFE images showed abundant 5 mm- to cm-sized marine snow aggregates. The BUOY-OSR collected only fragments of these aggregates and few particles larger than 2 mm.

Figure 10 shows cumulative volume attenuation size distributions corresponding to samples collected in January 2013 by the CFE and BUOY-OSR. We selected CFE images for depths 144 m (Fig. 7), 320, and 507 m. We also selected the BUOY-OSR image corresponding to Fig. 7 and another taken at the exact same time as the first CFE image. Other BUOY-OSR images were analysed for the rest of the time series. CFE images were either the first or second image after stage cleaning since subsequent images had multiple cases of particle overlap. BUOY-OSR images analysed were from just before stage cleaning since no particles were overlapping. Size distribution analysis was performed using ImageJ software, with an attenuation threshold  $>0.02$ , and a size threshold of at least two pixels for a particle. Particles were classified according to their equivalent circular diameter (ECD), with the lower size limit of  $20 \mu\text{m}$ . Volume attenuation for each particle was computed (the product of particle area and attenuation). Results were summed cumulatively from largest to smallest particle size and then normalized by total volume attenuation (Table 2; Fig. 10). In January 2013,  $>96\%$  of cumulative volume attenuation (CVA) was found in the  $>1000 \mu\text{m}$  size range in CFE data at all depths. In contrast, BUOY-OSR results typically show less than half of the cumulative volume attenuation in aggregates larger than  $1000 \mu\text{m}$ ; this is consistent with the particles being fragments of the larger aggregates and consistent with the factor of 20 difference in observed attenuation flux. If we were to eliminate all aggregates larger than  $1500 \mu\text{m}$  from January CFE data, then there is close agreement with the CVA – size-distributions derived from BUOY-OSR data. During the period when current flow across the BUOY-OSR fell below  $2 \text{ cm s}^{-1}$ , analysis of the BUOY-OSR image shows that nearly 50% of the aggregate volume attenuation was in the  $2000\text{-}5000 \mu\text{m}$ , i.e. large, size range. In other words, the surface tethered OSR began sampling larger aggregates.

Although, BUOY-OSR and CFE were operating at different depths, and separated by  $\sim 9 \text{ km}$  in our study area (Fig. 1), there was no indication in CTD/optics profiles that there was any discontinuity or advective feature at 237 m that would lead to biasing the BUOY-OSR results low. Nor was there any indication in remote sensing imagery (Supplemental materials) of nearby fronts or eddy structures. Furthermore, spatial chlorophyll variability was less than 20% in our study area (Appendix, Section 1.3).

Figure 11 shows CFE CVA – size distributions from all three expeditions compared with January BUOY-OSR data and further demonstrates that the CFE captured a greater loading of large particles than the BUOY-OSR. All lines of evidence indicate a major bias against aggregates larger than millimetre in size by the surface-tethered BUOY-OSR.

### 3.4 POC flux estimates

5 In absence of calibration sample data, calculations based on particle geometry, thickness, dry weight density, and organic matter percentages (Sec. 2.3 based on Bishop *et al.*, 1978) yield a scaling factor of 2.8, which can be used to convert the optical  $\text{POC}_{\text{ATN}}$  flux ( $\text{mATN}\cdot\text{cm}^2\cdot\text{cm}^{-2}\cdot\text{d}^{-1}$ ) to POC flux ( $\text{mmol C m}^{-2}\cdot\text{d}^{-1}$ ). POC flux was thus estimated to be 190, 240, and 100  $\text{mmol C m}^{-2}\cdot\text{d}^{-1}$  in Jan. 2013 (at 144, 320 and 506 m),  $\sim 18$   $\text{mmol C m}^{-2}\cdot\text{d}^{-1}$  in Mar. 2013 (from 170 to 508 m), and  $\sim 6$   $\text{mmol C m}^{-2}\cdot\text{d}^{-1}$  in May 2012 (430 to 900 m). We similarly estimate  $\sim 10$   $\text{mmol C m}^{-2}\cdot\text{d}^{-1}$  at 237  
10 m during the January 2013 BUOY-OSR deployment.

## 4. Discussion

### 4.1 Surface Biomass and Export in Coastal Waters

The high January 2013 POC flux values of 190 and 240  $\text{mmol C m}^{-2}\cdot\text{d}^{-1}$  to depths of 144 and 320 m are remarkable from several perspectives. Firstly, cases where the imaging stage was almost completely covered with material in 1.8  
15 hours had been never before encountered in our previous deployments of CFEs for missions totalling over 100 days (mostly in summer time conditions). Secondly, these high particle accumulation rates were observed in the wintertime at a time when both remotely-sensed and in-water optical measures of particle stocks were low. Thirdly, the magnitude of the January 2013 POC flux, estimated from CFE data, was approximately 8 times higher than the highest sedimentation rates measured using surface-tethered (at 100 and 200 m) and moored sediment traps (near 500  
20 m) in the nearby Santa Barbara (Thunnel, 1998; August 1993 to September 1996) and San Pedro Basins (Collins *et al.*, 2011; January 2004 through December 2007). In both these studies, POC flux in moored trap samples collected over 4 years at a depth of 500 m were typically 3  $\text{mmol C m}^{-2}\cdot\text{d}^{-1}$  with rare values as high as 15  $\text{mmol m}^{-2}\cdot\text{d}^{-1}$ . The much sparser surface-tethered trap observations (Collins *et al.*, 2011) were no higher than 28  $\text{mmol C m}^{-2}\cdot\text{d}^{-1}$ . The finding of high sedimentation rate during wintertime low-biomass conditions in California coastal waters has not  
25 been reported in multi-year moored sediment trap observations.

The May 2012 fluxes of 6  $\text{mmol m}^{-2}\cdot\text{d}^{-1}$  observed by CFE were the lowest of the study, at a time when surface waters had high particle concentrations, thus implying high recycling and shallow remineralisation. The finding of low export beneath plankton blooms in coastal waters reinforces the findings in the open ocean that high surface biomass does not imply high export to depth (Bishop and Wood, 2009; Lam and Bishop 2007; Ebersbach *et al.*, 2011).

30 The low surface biomass observed in January 2013 could indicate either a state of nutrient limitation of photosynthesis or a state of efficient transfer of primary produced organic matter to grazers and efficient particle export through the upper 500 m. We rule out nutrient limitation in our case, as mixed layers consistently shallower than 10 m and surface temperatures of 12.5 °C indicated that upwelling conditions were prevalent. Furthermore, we observed intense activity of marine mammals and sea birds feeding on abundant macro invertebrates and fish during

this period – which suggests that consumers were the source of the sinking aggregated material in the water column at this time. Many of the large aggregates seen in both Jan. and Mar. 2013 closely resemble abandoned appendicularian houses described by Alldredge and Silver (1988). Animations of CFE imagery are provided in supplemental materials for further exploration.

5 Physically driven aggregative processes were not likely in January and March 2013, as winds were below  $5 \text{ m s}^{-1}$  and averaged  $2.5 \text{ m s}^{-1}$ . In May 2012, winds were below  $10 \text{ m s}^{-1}$  and averaged  $3 \text{ m s}^{-1}$ . Surface waves and swell were almost completely absent in January and March. ADCP records showed currents were dominated by tidal fluctuations and not by eddy structures. The low biomass condition observed in January is therefore most consistent with biologically mediated export.

10 We note that 5-day running mean of satellite chlorophyll and POC levels appear to be nearly halved in a week (Fig. 6A,B) just before the study period in January. The decrease suggests that active grazing and export were in progress. Satellite imagery from Jan 2013 (Supplemental materials) shows a patchy POC/chlorophyll distribution without obvious eddy structures or fronts nearby.

Our observations show that  $\text{POC}_{\text{ATN}}$  flux profiles (Fig. 6) attenuate with depth, albeit not following the classic Martin et al. (1987) curve fit ( $\Phi_z = \Phi_{\text{Zref}}/(Z/\text{Zref})^b$ ,  $Z$  is depth,  $\text{Zref}=100 \text{ m}$  and  $\Phi$  is flux, and  $b = 0.858$ ). Using light based euphotic depths of 50, 20 and 25 m for January, March, and May as the  $\text{Zref}$  values for particle remineralisation (Buesseler and Boyd (2009), we derive Martin's 'b' factors of 0.36, 0.22, and 0.17, respectively, far lower than the accepted b value (Table 3). There are multiple limitations to this exercise; these include likely temporal variation of flux at a particular depth with time of day (see. e.g. Fig 15 in Bishop et al. 1987), depths sampled being 100 m deeper than the base of the euphotic zone, and the limited time of the study. This said, it is clear that in January 2013, the export may have been high enough to overwhelm the capacity of detritus feeders to reduce the flux. In May and March, all evidence is consistent with high recycling of the sinking POC in waters shallower than our 400 and 125 m observation points, respectively.

25 The fact that the PIC/POC ratio can decrease with depth suggests that carbonate dissolution may occur in shallow waters of the Pacific, a finding consistent with Bishop and Wood (2008). Also we note that living foraminifera and empty foraminifera shells were predominantly associated with large aggregates in January. While the occurrence of empty shells in aggregates would not be exceptional, the finding of living foraminifera suggests an active association with these particles.

#### 4.2 Surface tethered BUOY-OSR vs. Lagrangian CFE fluxes.

30 Our comparison of fluxes recorded by the CFE and a surface tethered BUOY-OSR in January 2013 found a factor of 20 difference in collection rate (Fig. 9), consistent with the loss of all aggregates  $>1500\mu\text{m}$  in size. CFE collection rates, ignoring the  $>1500 \mu\text{m}$  fraction in March 2013 and May 2012, would be approximately 4 times lower and 3 times lower, respectively (Fig. 11). This was surprising in light of reports that there are less than 'factor of two' differences in sedimentation measured using surface tethered particle interceptor traps (Martin et al. 1987; PITS) and neutrally-buoyant sediment traps (NBST) deployed in oligotrophic waters near Bermuda (Buesseler *et al.*, 2000; Stanley *et al.*, 2004, Owens *et al.*, 2013). In our study, the particles mostly absent from the BUOY-OSR were large

aggregates in the millimetre to cm size class (Figs. 9, 10, 11). The only time when large aggregates appeared in the BUOY-OSR imagery was during periods when the flow of water across the mouth of the BUOY-OSR was below 2 cm s<sup>-1</sup> (Fig. 8). Given that marine snow aggregates typically settle at rates of 0.1-0.2 cm s<sup>-1</sup> (Alldredge and Silver, 1988), the trajectory of the aggregates across the BUOY-OSR funnel would be almost horizontal, even in currents as weak as 2 cm/s. The large aggregates are thus likely discriminated against entering the cm-sized trap baffle openings, which are of the same size as the particles and we hypothesize that the aggregates simply bounce back into the flow after shedding a few fragments, rather than enter the trap.

Further support for a higher coastal sedimentation than is presently recognized is provided by Stukel et al. (2011) who worked just offshore of our study area in the California Current. They compared the new production (Eppley and Peterson, 1979) “f-ratio” – the fraction of primary production supported by upwelled nitrate vs. the <sup>234</sup>Th disequilibrium based “e-ratio” – the fraction of primary production exported as particles, and the two should be equivalent in a food web in equilibrium. While methods agreed 300 km offshore, the “f-ratio” exceeded the “e-ratio” by factors of 5-7 at locations within 50 and 100 km from the coast. Simply stated, there is insufficient time for the <sup>234</sup>Th (half life 24 days) deficit relative to its parent <sup>238</sup>U to reach steady state in coastal waters. Subsequent surface-tethered Particle Interceptor Trap deployments (Stukel et al., 2013) in the same area showed consistently low exports in this region where f-ratios are typically high (Eppley and Peterson, 1979). Our location is closer to shore. Even taking into account factors such as food web and lateral transport processes, multiple lines of evidence strongly indicates that large > 1 mm sized aggregates are severely under-sampled by surface-tethered baffled traps.

It is important to note that sediment traps have been the sole method to date for the assessment of carbon export in coastal waters. The single profile <sup>234</sup>Th/<sup>238</sup>U method is not applicable in the coastal environment since it relies on an assumption of a steady state deficit and requires a time scale of multiple half-lives (24.1 d) to reach this condition. Although the <sup>234</sup>Th/<sup>238</sup>U method may be used to infer export from time series sampling of a water parcel, such a study has not been undertaken in near-shore California waters to our knowledge. Also, e-ratio estimates are calibrated with large particles sampled either using traps or pumps and the assumption is that the Th:C ratio of all large particle phases is the same. Both methods have been shown to suffer serious biases; in-situ pumps are discussed by Bishop, Lam and Wood (2012), and results presented here show a serious issue of under sampling of large aggregates by surface tethered baffled traps. As there is scant literature on the size dependence of Th-C in different large particle size classes in the coastal environment, it is thus impossible to know the accuracy of e-ratio export estimates.

Coordinated at sea studies are required to inter compare the various methods of measurement of carbon export.

## 30 5. Conclusions

The new continuous observations of particulate flux off the coast of Southern California by autonomous CFE's show high fluxes in winter when surface chlorophyll is low. The finding is consistent with high primary productivity, efficient grazing, and high export of resulting aggregate material. The finding is also consistent with Eppley and Peterson's (1979) estimate of high new production and their inferred strength of particle export in near-shore waters, and as noted above, is higher by a factor of ~8 than the highest observations made with surface tethered and moored

sediment traps in waters close to our study site. Analysis of the images of accumulated particles suggest that surface-tethered sediment traps have under-sampled a major class of large aggregates contributing to carbon export from surface waters. At this writing, it is premature to revise the carbon export attributable to coastal waters up by a factor of 20 as we do not yet know the year-round contribution of large aggregates to sedimentation. In other seasons, our POC flux estimates are closer – but still elevated by greater than a factor of two compared with moored traps, and likely a minimum of a factor of three based on discussion of size frequency distribution results presented in Sec. 4.1. Missing contributions of large aggregates in sediment trap collections may explain the reported imbalance between POC flux to the seafloor and benthic respiratory demand seen at nearby station M (34° 50'N, 123° 00'W; Smith et al., 2013). We also show that particulate fluxes estimated using remotely sensed surface biomass may be overestimated sometimes - or underestimated at other times, depending on the population of grazers and the efficiency of export. The CFE can provide 'ocean truth' for such estimates.

There is uncertainty in the conversion of  $POC_{ATN}$  flux to POC flux, and we have no data on the conversion of  $PIC_{POL}$  to PIC flux; however, the optical metrics of POC and PIC flux are robustly defined for the CFE and the resulting images of settled particles clearly provide evidence of the food web mechanisms governing carbon export. Better calibration can only be achieved by at-sea 24-hour deployments of CFEs modified to collect samples; we hope to report on upcoming deployments soon.

While CFE and BUOY-OSRs were not directly compared with simultaneously measured fluxes with PIT traps, thorium methods, large particle abundances sampled by large volume in-situ filtration and other methods, such a study should be undertaken in biologically dynamic waters and augmented by a framework of contemporaneous remote sensing observations, water column biology and physics.

To date, two CFEs have each completed missions lasting 40 days offshore of California and another 10 days in the waters in the subarctic Pacific (mission duration set by ship availability) in bad weather and sea states, and without biofouling issues; our lab tests show that a CFE can perform hourly observations of carbon export in the open ocean for 8 months (2 hourly frequency for 16 months, etc...). More work to enable on board image data analysis is required to render the CFE fully autonomous.

Near shore, horizontal currents can displace a CFE from the area of intended operation in several days time; thus longer time series observations are difficult without a means to reposition the CFE. As the cost of a CFE is equivalent to the cost of operating a research vessel for ~2-3 days, the job of tending CFEs for seasonal or year round studies in the coastal environment would need to be done using autonomous surface or underwater vehicles.

In summary, we show that autonomous sampling technologies may be deployed to address many questions about the workings of the biological pump both offshore and onshore, including whether or not its strength has changed over the past several decades and whether or not it will change in the future in the face of anthropogenic  $CO_2$  warming and acidification, and exploitation of living resources of the ocean.

**Data Availability.** Data for plots, representative images used in this paper, and animations of image time series (at 1/2 resolution) are available as supplemental materials and are available from the author on request. Shipboard data sets: including

meteorological, surface hydrography, CTD cast data, are available through the Go Ship (<http://www.go-ship.org>) archives or in the case of ADCP data, are available through the University of Hawaii.

### **Acknowledgements.**

The CFE was developed in close collaboration with Mike McClune and Russ Davis of the Scripps Institution of Oceanography Instrument Development Group. OSR design and construction had critical contributions from the Electrical and Mechanical engineering groups and machine shop facilities at Lawrence Berkeley National Laboratory. Alex Morales (LBNL) and 25 UC Berkeley undergraduates facilitated CFE and BUOY-OSR deployments and recoveries at sea. In particular, Gabrielle Weiss, Amelia Weiss, Andrew Bower, and Christina Hamilton contributed both at sea and in the laboratory; we also thank the resident technicians, crews and captains of the R/V New Horizon for assistance. Jules Hummon (U Hawaii) assisted with ADCP data reprocessing. Hannah Bourne (UC Berkeley) cross-checked ADCP and BUOY-OSR current shear calculations. We thank Mati Kahru (SIO) for access to kilometre scale chlorophyll data for our study area. We thank the three anonymous reviewers for their contributions. The CFE data sets and animated image videos are posted as supplemental Information. Undergraduate participation in Cruises was facilitated by the UC Berkeley Undergraduate Research Apprentice Program and by the Earth and Planetary Science Department Ramsden fund. All work reported here was sponsored by National Science Foundation grant OCE-0936143 (JKBB).

### **Author contributions.**

JKBB initiated the CFE program, was chief scientist at sea, and led the analysis and writing of this paper. TJW played a key engineering role in all aspects of development, deployment, programming, and operation of the CFE. MBF analysed MODIS Aqua/Terra and VIIRS satellite data.

### **References.**

- Allredge, A.L. and Silver, M.W.: Characteristics, dynamics and significance of marine snow. *Prog. Oceanogr.* 20, 41–82, 1988.
- Armstrong, R. A., Lee, C., Hedges, J. I., Honjo, S. and Wakeham, S.G.: A new mechanistic model for organic carbon fluxes in the ocean based on quantitative association of POC with ballast minerals. *Deep-Sea Research Part II.* 49, 219-236, 2002.
- Asper, V.L.: Measuring the flux and sinking speed of Marine Snow Aggregates. *Deep-Sea Research* 34, 1-17, 1987.
- Banse, C.: Reflections About Chance in My Career, and on the Top-Down Regulated World. *Annu. Rev. Mar. Sci.* 5, 1–19, 2013.
- Be, A.W.H., Bishop, J.K.B., Sverdløve, M.S., and Gardner, W.D.: Standing Stock, Vertical Distribution, and Flux of Planktonic Foraminifera in the Panama Basin. *Marine Micropaleontology*, 9, 307-333, 1985.
- Bishop, J.K.B., Ketten, D.R. and Edmond, J.M. Chemistry, biology and vertical flux of particulate matter from the upper 400m of the Cape Basin in the Southeast Atlantic Ocean. *Deep-Sea Research* 25 (12), 1121–1161. 1978.

- Bishop, J.K.B., Stepien, J.C. and Wiebe, P.H.: Particulate matter distributions, chemistry and flux in the Panama Basin: response to environmental forcing. *Progress in Oceanography* 17, 1-59. 1987.
- Bishop, J.K.B., Wood, T. J., Davis, R. E. and Sherman, J. T.: Robotic Observations of Enhanced Carbon Biomass and Export at 55°S During SOFeX. *Science* 304, 417-420, 2004.
- 5 Bishop, J.K.B. and Wood, T.J.: Particulate Matter Chemistry and Dynamics in the Twilight Zone at VERTIGO ALOHA and K2 Sites. *Deep-Sea Research I* 55, 1684-1706. 10.1016/j.dsr.2008.07.012, 2008.
- Bishop, J.K.B. and Wood, T.J.: Year Round Observations of Carbon Biomass and Flux Variability in the Southern Ocean. *Global Biogeochemical Cycles*. 23. GB2019. doi:10.1029/2008GB003206. 2009.
- Bishop J.K.B., Lam, P.J. and Wood T.J.: Getting good particles: Accurate sampling of particles by large volume in-situ filtration. *Limnol. Oceanogr.: Methods* 10, 2012, 681–710. 2012.
- 10 Buesseler, K.O., Steinberg, D.K., Michaels, A.F., Johnson, R.J., Andrews, J.E., Valdes, J.R., Price, J.F.: A comparison of the quantity and composition of material caught in a neutrally buoyant versus surface-tethered sediment trap. *Deep-Sea Res. I* 47(2), 277–294. 2000.
- Buesseler, K. O., Antia, A. N., Chen, M., Fowler, S. W., Gardner, W. D., Gustafsson, O., Harada, K., Michaels, A. F., Rutgers van der Loeff, M., Sarin, M., Steinberg, D. K., and Trull, T.: An assessment of the use of sediment traps for estimating upper ocean particle fluxes. *Journal of Marine Research* 65, 345-416, 2007.
- 15 Buesseler, K. O. and Boyd, P. W.: Shedding light on processes that control particle export and flux attenuation in the twilight zone of the open ocean. *Limnology and Oceanography* 54, 1210-1232, 2009.
- Burd, A.B., Hansell, D.A., Steinberg, D.K., Anderson, T.R., Arístegui, J., Baltar, F., Beaufre, S.R., Buesseler, K.O., Dehairs, F., Jackson, G.A., Kadko, D.C., Koppelman, R., Lampitt, R.S., Nagata, T., Reinthaler, T., Robinson, C., Robison, B.H., Tamburini, C., and Tanaka, T.: Assessing the apparent imbalance between geochemical and biochemical indicators of meso-and bathypelagic biological activity: what the @\$#! is wrong with present calculations of carbon budgets? *Deep-Sea Research Part II* 57, 1557–1571, 2010.
- 20 Collins, L. E., Berelson, W., Hammond, D.E., Knapp, A., Schwartz, R., and Capone D.: Particle fluxes in San Pedro Basin, California: A four-year record of sedimentation and physical forcing. *Deep-Sea Research I* 58, 898–914, 2011.
- 25 Davis, R.E., Sherman, J. T. and Dufour, J.: Profiling ALACEs and other advances in autonomous subsurface floats. *J. Atmos. Oceanic Tech.* 18, 982-993, 2001.
- Ebersbach, F., Trull, T. W., Davies, D. M. and Bray, S. G.: Controls on mesopelagic particle fluxes in the Sub-Antarctic and Polar Frontal Zones in the Southern Ocean south of Australia in summer—Perspectives from free-drifting sediment traps *Deep-Sea Research II* 58. 2260–2276. 2011.
- 30 Eppley, R.W. and Peterson, B.J.: Particulate organic matter flux and planktonic new production in the deep ocean. *Nature* 282, 677-680. doi:10.1038/282677a0. 1979.
- Estapa, M.L., Buesseler, K., Boss, E. and Gerbi, G.: Autonomous, high-resolution observations of particle flux in the oligotrophic ocean. *Biogeosciences*, 10, 5517–5531, 2013.
- 35 Field, C. B., Behrenfeld, M. J., Randerson, J. T. and Falkowski, P. G.: Primary production of the biosphere: Integrating terrestrial and oceanic components, *Science* 281, 237-240. 1998,
- Henson, S. A., Sanders, R., Madsen, E., Morris, P. J., Le Moigne, F., and Quartly G. D.: A reduced estimate of the strength of the ocean’s biological carbon pump, *Geophys. Res. Lett.*, 38, L04606, doi:10.1029/2011GL046735. 2011.
- Gardner, W.D.: Sediment trap sampling in surface waters. In Hanson, Ducklow, H. and Field, C. eds. *The Changing Ocean Carbon Cycle: A midterm synthesis of the Joint Global Ocean Flux Study*. Cambridge Univeristy Press. 240-284, 2000.
- 40 Guay, C.K. and Bishop, J.K.B.: A rapid birefringence method for measuring suspended CaCO<sub>3</sub> concentrations in water, *Deep-Sea Research I* 49, 197-210, 2002.
- Hedges, J.I., Baldock, J.A., Gelin, Y., Lee, C., Peterson, M.L., and Wakeham, S.G.: The biochemical and elemental compositions of marine plankton: a NMR perspective. *Marine Chemistry* 78 (1), 47–63, 2002.
- 45 Hummon, J.M. and Firing, E.: A direct comparison of two RDI shipboard ADCPs: a 75-kHz Ocean Surveyor and a 150-kHz Narrowband. *J. Atmos. and Oceanic Technol.*, 20, 872–888. 2003.

- Kahru, M., Kudela R.M., Manzano-Sarabia M., and Mitchell B.G.: Trends in the surface chlorophyll of the California Current: Merging data from multiple ocean color satellites, *Deep-Sea Research. II*, 77-80, 89-98, 2012
- Lam, P. J. and Bishop, J. K. B.: High Biomass Low Export regimes in the Southern Ocean. *Deep-Sea Research II* 54, 601-638. doi:10.1016/j.dsr2.2007.01.013. 2007.
- 5 Lampitt, R.S., Boorman, B., Brown, L., Lucas, M., Salter, I., Sanders, R., Saw, K., Seeyave, S., Thomalla, S. J., and Turnewitsch, R.: Particle export from the euphotic zone: estimates using a novel drifting sediment trap, Th-234 and new production. *Deep-Sea Research Part I* 55 (11), 1484–1502, 2008.
- Lee, C., Peterson, M.L., Wakeham, S.G., Armstrong, R.A., Cochran, J.K., Miquel, J.C., Fowler, S.W., Hirschberg, D., Beck, A., and Xue, J.: Particulate organic matter and ballast fluxes measured using time-series and settling velocity sediment traps in the northwestern Mediterranean Sea. *Deep-Sea Res. II* 56 (18), 1420-1436. 2009.
- 10 Martin, J.H., Knauer, G.A., Karl, D.M. and Broenkow, W.W.: VERTEX: carbon cycling in the northeast Pacific. *Deep-Sea Research* 34, 267-285, 1987.
- Owens, S.A., Buesseler, K.O., Lamborg, C.H., Valdes, J., Lomas, M.W., Johnson, R.J., Steinberg, D.K. , and Siegel, D.A.: A new time series of particle export from neutrally buoyant sediments traps at the Bermuda Atlantic Time-series Study site. *Deep-Sea Research I*, 72, 34–47, 2013.
- 15 Siegel, D. A., Buesseler, K.O., Doney, S.C., Sailley, S.F., Behrenfeld, M.J., and Boyd, P.W.: Global assessment of ocean carbon export by combining satellite observations and food-web models, *Global Biogeochem. Cycles* 28, doi:10.1002/2013GB004743. 2014.
- Smith, K. L., Ruhl, H.A., Kahru, M., Huffard, C.L. and Sherman, A.D.: Deep ocean communities impacted by changing climate over 24 y in the abyssal northeast Pacific Ocean. *Proc. Natl. Acad. Sci.* 110 (49). doi/10.1073/pnas.1315447110. 2013.
- 20 Stanley, R.H.R, Buesseler, K.O., Manganini, S.J., Steinberg, D.K. and Valdes, J.R.: A comparison of major and minor elemental fluxes collected in neutrally buoyant and surface-tethered sediment traps. *Deep-Sea Research I* 51, 1387-1395. 2004.
- 25 Stukel, M.R., Landry, M. R., Benitez-Nelson, C. R. and Goericke, R.: Trophic cycling and carbon export relationships in the California Current Ecosystem. *Limnol. Oceanogr.*, 56(5), 1866–1878. doi:10.4319/lo.2011.56.5.1866. 2011.
- Stukel, M.R., Ohman, M.D., Benitez-Nelson, C. R. and Landry, M. R.: Contributions of mesozooplankton to vertical carbon export in a coastal upwelling system. *Mar. Ecol. Prog. Ser.* 491, 47-65. doi: 10.3354/meps10453. 2013.
- 30 Thunell, R.C.: Particle fluxes in a coastal upwelling zone: sediment trap results from Santa Barbara Basin, California. *Deep-Sea Research Part II* 8–9,1863–1884, 1998.
- Turner, J.T.: Zooplankton fecal pellets, marine snow, phytodetritus and the ocean’s biological pump. *Prog. Oceanogr.* 130, 205–248, 2015.
- Volk, T., and Hoffert, M.I.: Ocean carbon pumps: analysis of relative strengths and efficiencies in ocean-driven atmospheric CO<sub>2</sub> changes. *Geophysical Monographs* 32, 99–110. 1985.
- 35 Yao, X. and Schlitzer, R.: Assimilating water column and satellite data for marine export production estimation. *Geosci. Model Dev.* 6, 1575–1590. 2013.

## Appendix A. Methods Detail

### 40 A1.1 Optical Sedimentation Recorder on CFE.

The Optical Sedimentation Recorder (OSR; *Fig. A1*) is independently powered from the SOLO float to which it is attached and the two communicate via a hard-wired link. It thus does not impact the number of profiles that the float can make beyond additional telemetry needs.

The SOLO dives to its target depth and signals the OSR to begin operation. During time at depth, particles settle into a baffled (5 cm thick x 1 cm opening hex cell) high aspect polished titanium funnel (height 23.6 cm; slope 75°; 15.4 cm diameter opening) and settling column (height ~11 cm) before depositing on a 2.5 cm diameter glass sample stage. The baffle is typical to the dimensions used in surface tethered Particle Interceptor Traps (e.g. Martin et al. 1987, Collins et al., 2011, Stukel et al., 2013).

A downward focused 5 cm diameter white (color temperature 2700 K) light emitting diode (LED) source with bonded linear polarizer (Meadowlark Optics, Frederick, CO) is axially aligned with the funnel and provides transmitted light (or backlit) illumination of the sample.

An annular array of 12 white LEDs provides dark field illumination. This light source is integrated within the body of a 3-D printed form designed to provide both a hydrodynamic cleaning function and to secure a 27 mm diameter dashed cross-hair reticle (Edmond Optics Inc., Barrington, NJ) to the pressure case window. A Seabird Inc. (Bellevue WA) pump outfitted with an isolation valve is used to flush the sample stage during cleaning.

A substage polarizer rotator is rotated either parallel or perpendicular to the axis of the downlight polarizer. In the case of CFE001, this polarizer rotator was housed within the instrument pressure case.

Under computer control, particles are imaged with a 5M pixel Sumix (SMX-11M5C; Oceanside, CA) colour imager in transmitted, transmitted – cross polarized, and dark field lighting modes which are designated as TRA, POL, DRK, respectively. Gain settings for each of the red, green, blue (RGB) channels were adjusted so that images of the downlight yield similar count value histogram averages (to within several %). The same gain settings were used for cross-polarized transmitted light illumination. For dark field, RGB channel balance was achieved by imaging salt crystals dispersed across the sample stage. The camera lens was set to F16. Shutter timing was set for each of the three modes to prevent image saturation.

#### **A 1.2 Surface conditions, Hydrography, and Transmissometer data.**

Sea and wind conditions during the three study periods were benign. For example, In January and March 2013, winds monitored by the ship were less 5 m s<sup>-1</sup> and averaged 2.5 m s<sup>-1</sup>. In May 2012, winds were less than 10 m s<sup>-1</sup> and averaged 3 m s<sup>-1</sup>. Surface waves and swell were almost completely absent in January and March. In January 2013, the weather was completely cloud free which contributed to excellent satellite imagery of the area.

During all expeditions, a CTD/rosette system with a C-Star (WETLabs, Inc. Philomath, OR) transmissometer and Seapoint Inc. scattering sensor was repeatedly deployed to full water column depth. Approximately 20 casts were completed during each cruise. Only transmissometer data are reported here. The transmissometer cleaning, calibration and data processing to particle beam attenuation coefficient ( $c_p$ ) follow protocols we have published (Bishop and Wood, 2008, Bishop, Lam and Wood, 2012). POC was calculated by multiplying particle beam attenuation coefficient by 27 (Bishop and Wood, 2008).

Figure A2 (A-C) shows  $c_p$  profiles for the three expeditions. Also shown is 0-20 m averaged POC from these casts. The time line for plot (D) is relative to the start of deployment of the CFE. Average and standard deviation values of 0-20 m averaged POC are quoted in the text.

The effects of internal waves with periods of 20-30 minutes were usually seen in CTD cast data. In March 2013, internal wave amplitudes of approximately 40 m were observed during CTD tow-yo experiments. During other expeditions, wave amplitudes were less than 20 m.

### **A 1.3 Spatial gradients of surface chlorophyll in the study area.**

5 To examine the detailed spatial gradients of chlorophyll in our study area, we chose locations at 33.73°N 119.50°W and 33.69°N 119.58°W and retrieved chlorophyll data at 1 km spatial resolution within a 2 km search radius of the two locations. These positions were 9 km apart. To achieve greater temporal and spatial coverage than possible with the single MODIS/Aqua product, we analysed merged data from MODIS on the Aqua and Terra satellites and from the Visible Infrared Imaging Radiometer Suite (VIIRS) on the National Polar-orbiting Partnership Suomi satellite  
10 (Kahru et al. 2012; [http://spg.ucsd.edu/Satellite\\_Data/California\\_Current/](http://spg.ucsd.edu/Satellite_Data/California_Current/)). Images at 1 km resolution are provided in Supplemental material.

Figure A3 shows time series of daily mean and standard deviation of chlorophyll plotted for both locations over thirty day periods encompassing the days that the ship was on station in the Santa Cruz Basin and during CFE  
15 deployments. Also plotted is the relative difference in chlorophyll between the two locations. The two locations were almost always <20% different from one another. From this we conclude that a separation of 9 kilometers is not a significant cause of differences in our data. In other words, spatial gradients of biomass in our study area were small.

### **A 1.4 BUOY-OSR configuration, January 2013.**

Figure A4 depicts the deployment configuration of the sample collecting BUOY-OSR used in this study. A SBE 19-  
20 plus logging CTD (Sea Bird Electronics, Bellevue WA) recorded pressure, temperature and salinity at 5 second intervals. One OSR (Buoy instrument 84) was configured identically to CFE001. The funnel assembly of the second OSR (Buoy instrument 88) had a sample stage leak enabling strong water circulation through the funnel leading to particle loss as the system was pumped up and down due to wave action. Buoy instrument 84 is considered reliable as particles remained in place where they fell as they accumulated.

25

**Table 1. Carbon Flux Explorer and BUOY-OSR positions**

Carbon Flux Explorer Surfacing Positions				
Dive	Date	Time (UTC)	Longitude	Latitude
123	1-Jun-2012	3:15	-119.475	33.738
124	1-Jun-2012	11:49	-119.479	33.731
125	1-Jun-2012	21:14	-119.484	33.736
126	2-Jun-2012	4:52	-119.480	33.744
127	2-Jun-2012	13:28	-119.498	33.744
128	2-Jun-2012	22:48	-119.492	33.750
129	3-Jun-2012	6:24	-119.493	33.737
130	3-Jun-2012	15:10	-119.508	33.740
132	3-Jun-2012	20:45	-119.512	33.735
143	19-Jan-2013	8:16	-119.479	33.744
144	19-Jan-2013	9:13	-119.484	33.744
145	19-Jan-2013	16:31	-119.514	33.744
146	19-Jan-2013	23:45	-119.522	33.722
147	20-Jan-2013	8:21	-119.575	33.714
148	20-Jan-2013	14:52	-119.600	33.695
150	20-Jan-2013	20:46	-119.605	33.667
161	28-Mar-2013	10:55	-119.537	33.709
162	28-Mar-2013	18:19	-119.529	33.709
163	29-Mar-2013	4:08	-119.555	33.705
164	29-Mar-2013	10:47	-119.586	33.687
165	29-Mar-2013	18:05	-119.576	33.693
166	30-Mar-2013	3:02	-119.607	33.696
167	30-Mar-2013	9:46	-119.614	33.673

BUOY-OSR Positions January 2013				
Date	Time (UTC)	Longitude	Latitude	
20-Jan-2013	9:00	-119.490	33.740	
20-Jan-2013	10:00	-119.496	33.739	
20-Jan-2013	11:00	-119.501	33.739	
20-Jan-2013	12:00	-119.507	33.739	
20-Jan-2013	13:00	-119.513	33.740	
20-Jan-2013	14:00	-119.519	33.741	
20-Jan-2013	15:00	-119.524	33.742	
20-Jan-2013	16:00	-119.530	33.744	
20-Jan-2013	17:00	-119.534	33.745	
20-Jan-2013	18:00	-119.538	33.746	
20-Jan-2013	19:00	-119.542	33.747	
20-Jan-2013	20:00	-119.545	33.748	
20-Jan-2013	21:00	-119.546	33.749	
20-Jan-2013	22:00	-119.548	33.748	
20-Jan-2013	23:00	-119.550	33.747	

**Table 2. Volume Attenuance Size Distributions for CFE and BUOY-OSR Samples from January 2013.**

Diameter <sup>1</sup> ( $\mu\text{m}$ )	144 m CFE		320 m CFE		507 m CFE		237 m BUOY <sup>2</sup>			237 m BUOY <sup>3</sup>	
	20130120 11:11		20130120 16:42		20130120 05:56		20130120 AVG			20130120 18:08	
>5000	0.462 <sup>4</sup>	0.462 <sup>5</sup>	0.000	0.000	0.776	0.776	0.000	0.000	$\pm 0.000$	0.000	0.000
2000-5000	0.441	0.903	0.978	0.978	0.150	0.926	0.065	0.065	$\pm 0.130$	0.494	0.494
1000-2000	0.059	0.962	0.000	0.978	0.055	0.981	0.353	0.418	$\pm 0.090$	0.169	0.662
500-1000	0.014	0.976	0.007	0.984	0.003	0.983	0.250	0.668	$\pm 0.070$	0.153	0.815
200-500	0.015	0.992	0.005	0.989	0.011	0.994	0.245	0.913	$\pm 0.022$	0.144	0.959
100-200	0.005	0.996	0.007	0.996	0.003	0.997	0.064	0.977	$\pm 0.006$	0.030	0.989
50-100	0.003	0.999	0.003	0.999	0.002	0.999	0.017	0.994	$\pm 0.001$	0.008	0.997
20-50	0.001	1.000	0.001	1.000	0.001	1.000	0.006	1.000	$\pm 0.000$	0.003	1.000

- 5
1. Diameter is Equivalent Circular Diameter of particle with the same area;
  2. Averages (excluding 18:08 data) for BUOY data, third column ( $\pm$ ) is s.d. of cumulative data.
  3. Currents below 3 cm/sec for 60 min.
  4. Volume Attenuance for indicated size interval.
  5. Cumulative volume attenuance for particles greater than lower limit of size interval

10

**Table 3. Martin curve fit parameters**

Time	Zref (m)	$\Phi_{Zref}^1$	b	Std. Dev. <sup>1</sup>	$\Phi_{Zref}$	b	Std. Dev.
Jan. 2013	50	252.0	0.858	34.7	115.0	0.36	23.3
Mar. 2013	20	57.5	0.858	2.3	11.4	0.22	0.4
May 2012	25	35.0	0.858	1.0	3.8	0.17	0.6

1. Units are in  $\text{mATN-cm}^2 \text{ cm}^{-2}$

## Figure Captions.

Figure 1. Left. Carbon Flux Explorer showing the SOLO float and interfaced Optical Sedimentation Recorder. Top Right: Relief Map for Southern California Bight (Google Earth) centered on the Santa Cruz Basin (SCB) and our study area (shown in yellow). Also shown are locations of moored sediment trap deployments in the Santa Barbara Basin (SBB, Thunnel, 1998), and San Pedro Basin (SPB, Collins et al. 2011). Lower Right: Operations within study area. Surfacing positions of CFE001 during May 2012 (red triangles), Jan. 2013 (blue circles) and Mar. 2013 (Green box) - Also shown is track for the BUOY-OSR system (blue line) in Jan. 2013; separation of CFE and BUOY-OSR was approximately 9 km. Small symbols denote locations of CTD Casts. All motion was to the southwest. CFE and BUOY-OSR deployments took near 33.75°N 119.5°W. CTD profiles were taken within several km of CFE and BUOY-OSR positions.

10

Figure 2. Detail of Image Analysis Scheme for CFE and BUOY-OSR images. Images from NH1301 CFE001 deployment. (A) Raw Backlit (TRA) images are divided by the in-situ TRA lighting reference (Cross hair reticle has 1 mm sized dashes) to get transmittance. This image is transformed to units of attenuation. (B) Raw crossed polarized transmitted light [POL] image is first corrected for attenuation effects of optically dense particles by dividing by PCF, an empirically derived factor proportional to attenuation (ATN). The POL lighting REF is then subtracted and then divided by the TRA Lighting ref to yield the normalized POL image. The contrast and brightness of the final image is enhanced. (C). Raw Dark Field (DRK) images are normalized by dividing by the in-situ lighting reference intensity.

Figure 3. Magnified detail of a marine snow aggregate from the upper left hand quadrant after processing to normalized Dark Field (DRK) counts, Attenuance (ATN), and polarized (POL) counts. The scale of the aggregate is ~1 cm. Image resolution is 13  $\mu\text{m}$ . An empty 600  $\mu\text{m}$  Pteropod shell is at the bottom left of the POL image. The 10 bright spherical regions in the POL image are ~200  $\mu\text{m}$  sized Foraminifera shells; haze in aggregates is likely due to coccoliths.

Figure 4. Results from CFE deployments in the Santa Cruz Basin. CFE depths shown in italics. (A) sample attenuation from transmitted light images. (B) polarized photon yield in parts per million from cross-polarized light images. Small circles denote the time that the images were taken. The sawtooth pattern registers particle accumulation and drops to baseline at the time of stage cleaning.

Figure 5.  $\text{POC}_{\text{ATN}}$  (A) and  $\text{PIC}_{\text{POL}}$  (B) flux systematics from CFE deployments in the Santa Cruz Basin. CFE depths are shown in italics in (A). Bars and small circles denote average flux over 1.8 and 0.3 hour intervals, respectively.

Figure 6. A) Chlorophyll-a and POC from the MODIS Aqua satellite; lines are 5 point running means. Color scheme for May 2012 (red), Jan. 2013 (blue) and March 2013 (green). Open and filled graphics in A and B correspond to the week previous to and during each expedition. (B) From left to right successive bar pairs depict satellite chlorophyll and satellite POC. Crosshatched bars denote 0-20 m transmissometer POC. (C)  $\text{POCATN}$  flux for January (blue circles), March (green squares), and May (red triangles). The large filled symbols are a grand average for a particular depth, small open symbols denote 1.6 hour averaged data. (D)  $\text{PICPOL}$  flux profiles. Symbols as in C.

Figure 7. Depth profiles of the ratio of PIC and POC flux proxys. Results show highest relative contribution of PIC occurred in March 2013. January and May values near 500 m are comparable.

Figure 8. Time series of image attenuation from CFE and BUOY-OSR deployments in the Santa Cruz Basin during January 2013. Time axis is elapsed days since January 1 at 0000 UTC. In (A) and (B), the green lines depict the ATN time series. In (B), red symbols depict currents relative to the BUOY-OSR at a depth of 237 m that were calculated using ship broad band acoustic current profiler data (RDI Instruments, Ocean Surveyor 75; methods described by Hummon and Firing (2003) and 30 minute BUOY-OSR GPS positions. The current dropped briefly below 1 cm s<sup>-1</sup> and the rate of accumulation of particles in the BUOY-OSR increased. This moment was also the time when the first large aggregates were seen. Also shown in (B) in blue is the temperature time series from the logging CTD. The most obvious effect on particle collection rate by the BUOY-OSR was the relative lull in currents near day 19.68. Images from samples depicted by \* are compared in Figure 9. (C) Time series of CFE and BUOY-OSR tilt in degrees. CFE tilt averaged 3 degrees, whereas BUOY-OSR tilt averaged 0.5 degrees.

Figure 9. Comparison of representative Dark Field Images of accumulated settling particles over a 2.5 hour period from an Optical Sedimentation Recorder (OSR) on the Carbon Flux Explorer (CFE, upper left) vs. that from a surface BUOY-tethered OSR (upper right) during NH1301 (Jan. 2013). The CFE was observing sedimentation at 320 m (image 21:14 UTC). The BUOY-OSR was deployed at 237 m (image 18:07 UTC). Each image is 2.5 cm across and pixel resolution is 14 μm. The Large fluffy 0.5 – 1.0 cm sized marine snow aggregates were almost completely missed by the BUOY OSR. Winds were near calm (< 5 m s<sup>-1</sup>) and surface waves and swell were almost entirely absent. The BUOY system had ~0.5° of tilt. The only difference between the CFE and BUOY was the absence/presence of tidally fluctuating horizontal currents of up to 8 cm sec<sup>-1</sup>. Only fragments of the marine snow particles were seen in the BUOY samples.

Figure 10. Comparison of Normalized Cumulative Attenuance – Size Distribution (NCA-SD) for images from CFE and BUOY-OSR systems, January 2013. Over 96% of the cumulative volume attenuation loading was in the >1000 μm fraction in CE samples. The BUOY system images at 11:26 and 18:08 corresponded to times when current velocity above the mouth of the trap was 6 cm s<sup>-1</sup> and less than 2 cm s<sup>-1</sup>, respectively. The cumulative distributions for the BUOY-OSR can be matched by eliminating all of the >1500 μm sized material from the CFE size distributions.

Figure 11. Comparison of Normalized Cumulative Volume Attenuance – Size Distributions (CVA-SD) from CFE deployments in May 2012 (red lines and symbols), January 2013 (blue), and March 2013 (green). Shown in black is the average CVA-SD from BUOY-OSR deployments. No CFE data from any of the three expeditions overlapped BUOY-OSR results from January 2013; in all cases, larger particles were observed by the CFE.

Figure A1. Drawing depicting the configuration of CFE001 and detail of lighting/imaging elements of the Optical Sedimentation Recorder (OSR). During operation, the OSR uses a 3 axis accelerometer to monitor system tilt.

Figure A2. (A-C) Particle beam attenuation coefficient ( $c_p$ ) profiles corresponding to NH1301 (Jan 2013), NH1304 (Mar. 2013), and NH1204 (May/June 2012) Expeditions. (D) POC calculated for the 0-20 m depth interval using  $c_p$  multiplied by 27. The x axis is in days relative to the start of each CFE deployment.

Figure A3. Left Panels: Means and standard deviations of chlorophyll a retrieved from 1 km spatially resolved merged MODIS Aqua/Terra and VIIRS Sumoi products within 2 km radius of 33.73N, 119.50W (red triangles) and 33.69N 119.58W (blue

circles). Top to bottom graphs correspond to times of sampling. Dashed blue lines denote the periods that the ship was on station in the Santa Cruz Basin study area. The black horizontal line denotes duration of CFE deployments. Right panels show the fractional difference in mean chlorophyll between the two locations. There was no systematic difference between locations.

Figure A4. Photograph of the surface tethered BUOY-OSR as deployed in January 2013. Also shown is the mooring configuration used in this study. The seven small floats spaced 1 m apart are intended to minimize the effects of surface wave action on the up and down motion of the subsurface sediment trap. During the January 2013 deployment depth was 237 m ( $\pm 0.25$  m S.D.) – Maximum peak to trough vertical motion was 1 m.

10

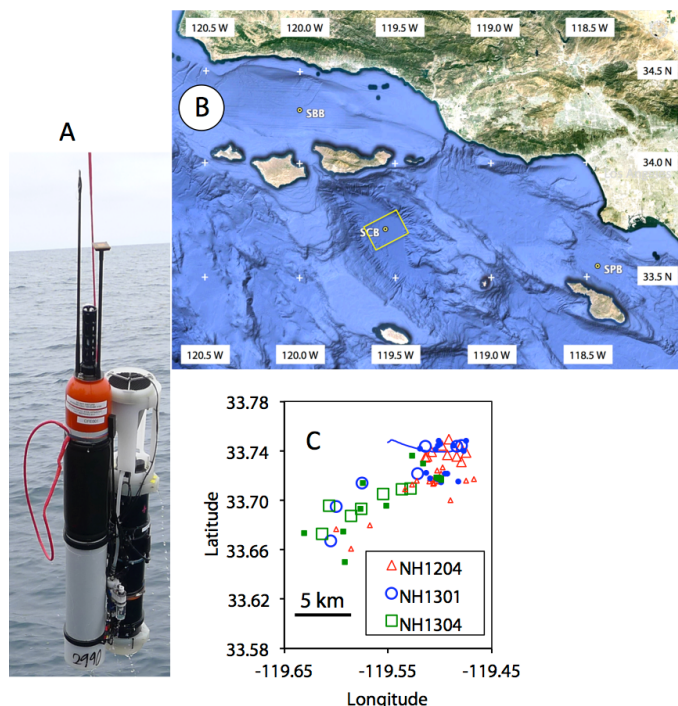


Figure 1. Left. Carbon Flux Explorer showing the SOLO float and interfaced Optical Sedimentation Recorder. Top Right: Relief Map for Southern California Bight (Google Earth) centered on the Santa Cruz Basin (SCB) and our study area (shown in yellow). Also shown are locations of moored sediment trap deployments in the Santa Barbara Basin (SBB, Thunnel, 1998), and San Pedro Basin (SPB, Collins et al. 2011). Lower Right: Operations within study area. Surfacing positions of CFE001 during May 2012 (red triangles), Jan. 2013 (blue circles) and Mar. 2013 (Green box) - Also shown is track for the BUOY-OSR system in Jan. 2013; separation of CFE and BUOY-OSR was approximately 9 km. Small symbols denote locations of CTD Casts. All motion was to the southwest.

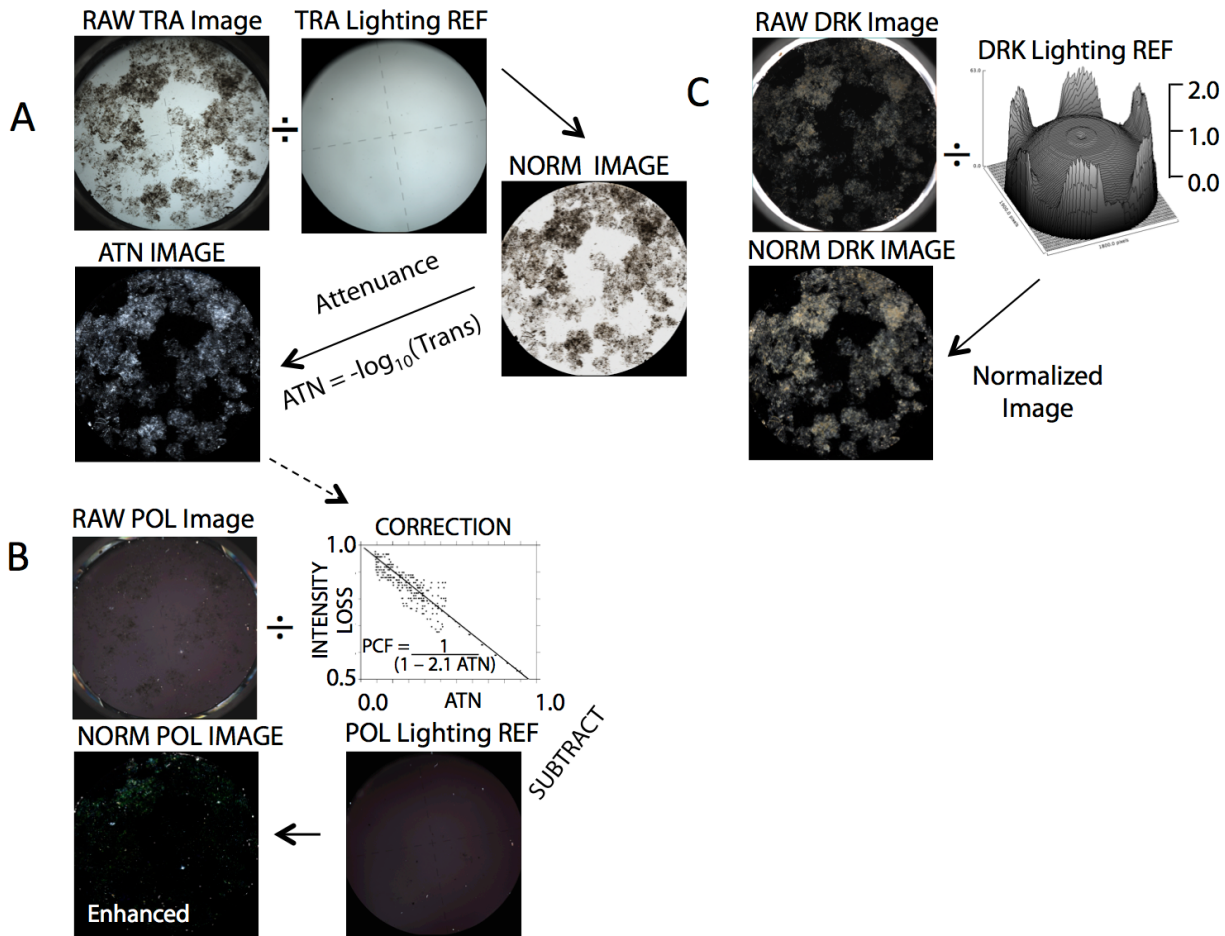
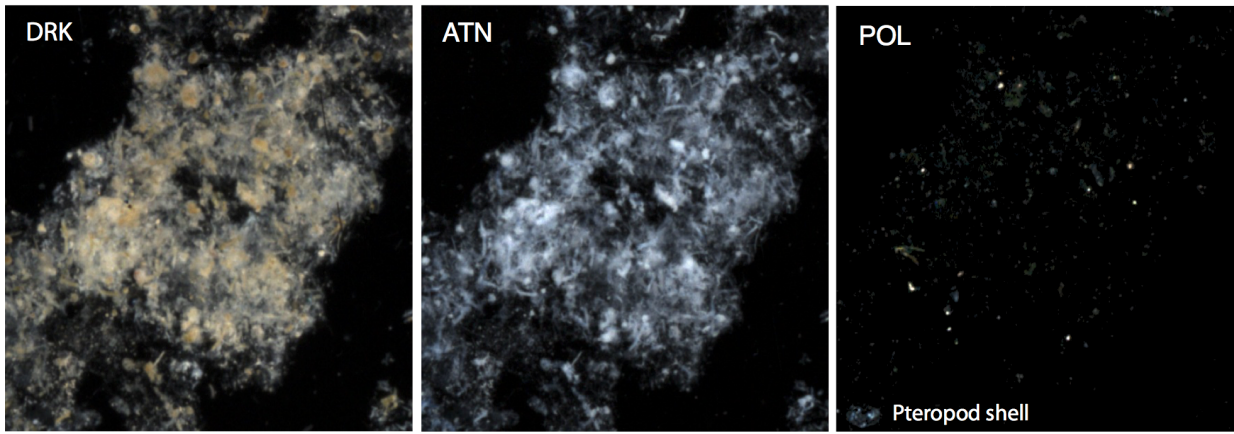


Figure 2. Detail of Image Analysis Scheme for CFE and BUOY-OSR images. Images from NH1301 CFE001 deployment. (A) Raw Backlit (TRA) images are divided by the in-situ TRA lighting reference (Cross hair reticle has 1 mm sized dashes) to get transmittance. This image is transformed to units of attenuation. (B) Raw crossed polarized transmitted light [POL] image is first corrected for attenuation effects of optically dense particles by dividing by PCF, an empirically derived factor proportional to attenuation (ATN). The POL lighting REF is then subtracted and then divided by the TRA Lighting ref to yield the normalized POL image. The contrast and brightness of the final image is enhanced. (C). Raw Dark Field (DRK) images are normalized by dividing by the in-situ lighting reference intensity.



5 Figure 3. Magnified detail of a marine snow aggregate from the upper left hand quadrant after processing to normalized Dark Field (DRK) counts, Attenuance (ATN), and polarized (POL) counts. The scale of the aggregate is ~1 cm. Image resolution is better than 15  $\mu\text{m}$ . An empty 600  $\mu\text{m}$  Pteropod shell is at the bottom left of the POL image. The 10 bright spherical regions in the POL image are ~200  $\mu\text{m}$  sized Foraminifera shells; haze in aggregates is likely due to coccoliths.

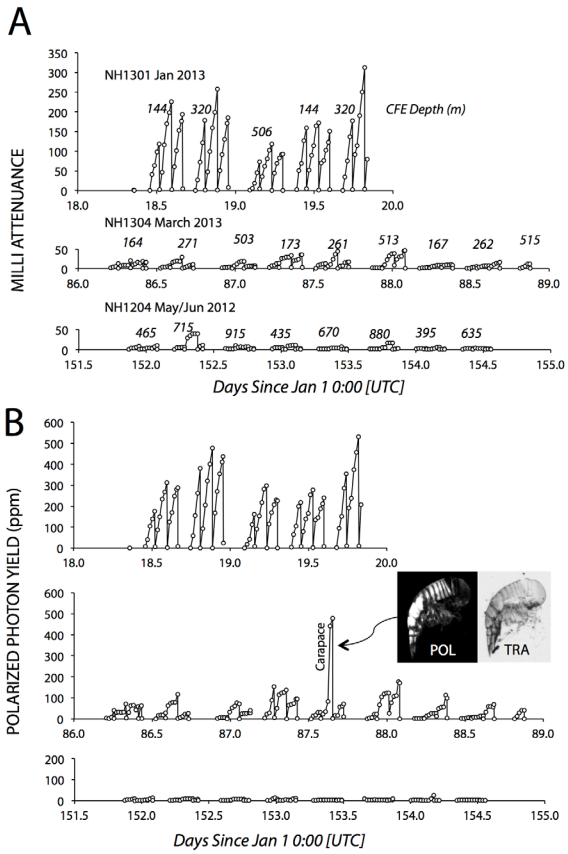


Figure 4. Results from CFE deployments in the Santa Cruz Basin. CFE depths shown in *italics*. (A) sample attenuation from transmitted light images. (B) polarized photon yield in parts per million from cross-polarized light images.

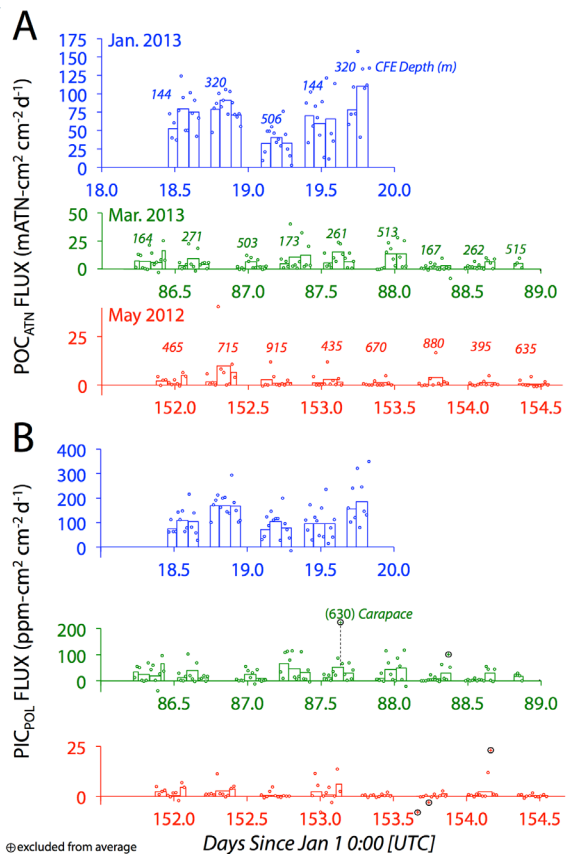


Figure 5. POC<sub>ATN</sub> (A) and PIC<sub>POL</sub> (B) flux systematics from CFE deployments in the Santa Cruz Basin. CFE depths are shown in italics in (A). Bars and small circles denote average flux over 1.8 and 0.3 hour intervals, respectively.

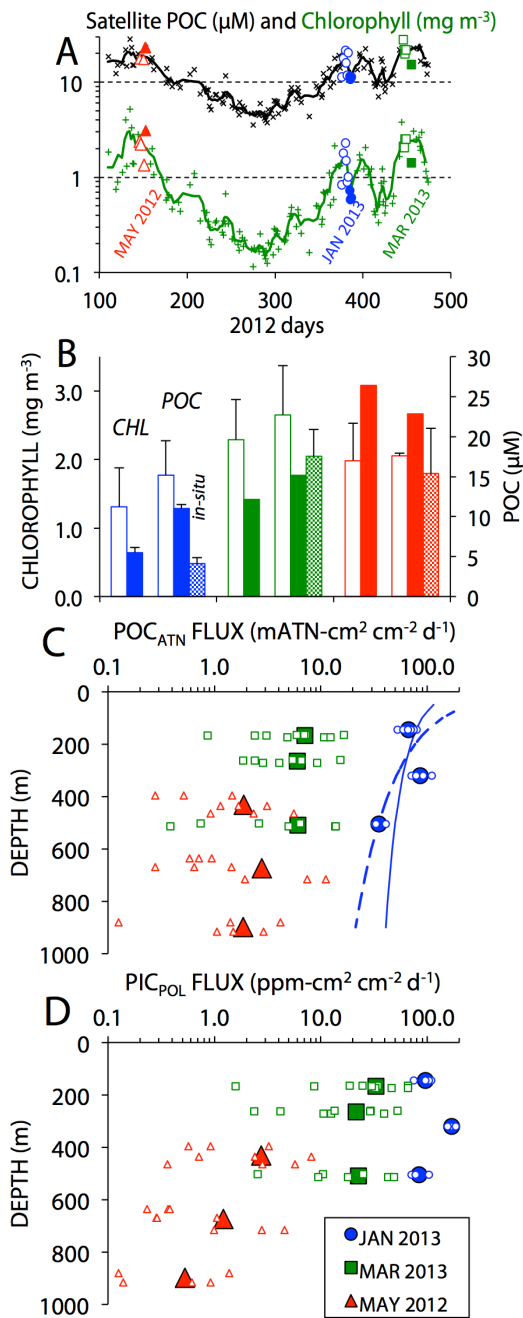


Figure 6. A) Chlorophyll-a and POC from the MODIS Aqua satellite; lines are 5 point running means. Color scheme for May 2012 (red), Jan. 2013 (blue) and March 2013 (green). Open and filled graphics in A and B correspond to the week previous to and during each expedition. (B) From left to right successive bar pairs depict satellite chlorophyll and satellite POC. Crosshatched bars denote 0-20 m transmissometer POC. (C)  $\text{POC}_{\text{ATN}}$  flux for January (blue circles), March (green squares), and May (red triangles). The large filled symbols are a grand average for a particular depth, small open symbols denote 1.6 hour averaged data. Dashed and solid blue lines denote Martin curve fits with  $B=0.858$  and  $0.31$ , respectively, (D)  $\text{PIC}_{\text{POL}}$  flux profiles. Symbols as in C.

Figure 7.

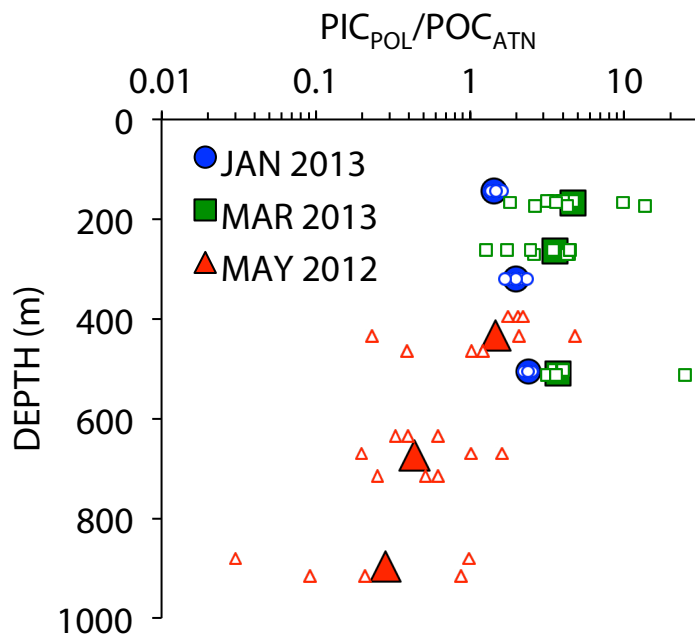


Figure 7. Depth profiles of the ratio of PIC and POC flux proxys. Results show highest relative contribution of PIC occurred in  
5 March 2013. January and May values near 500 m are comparable.

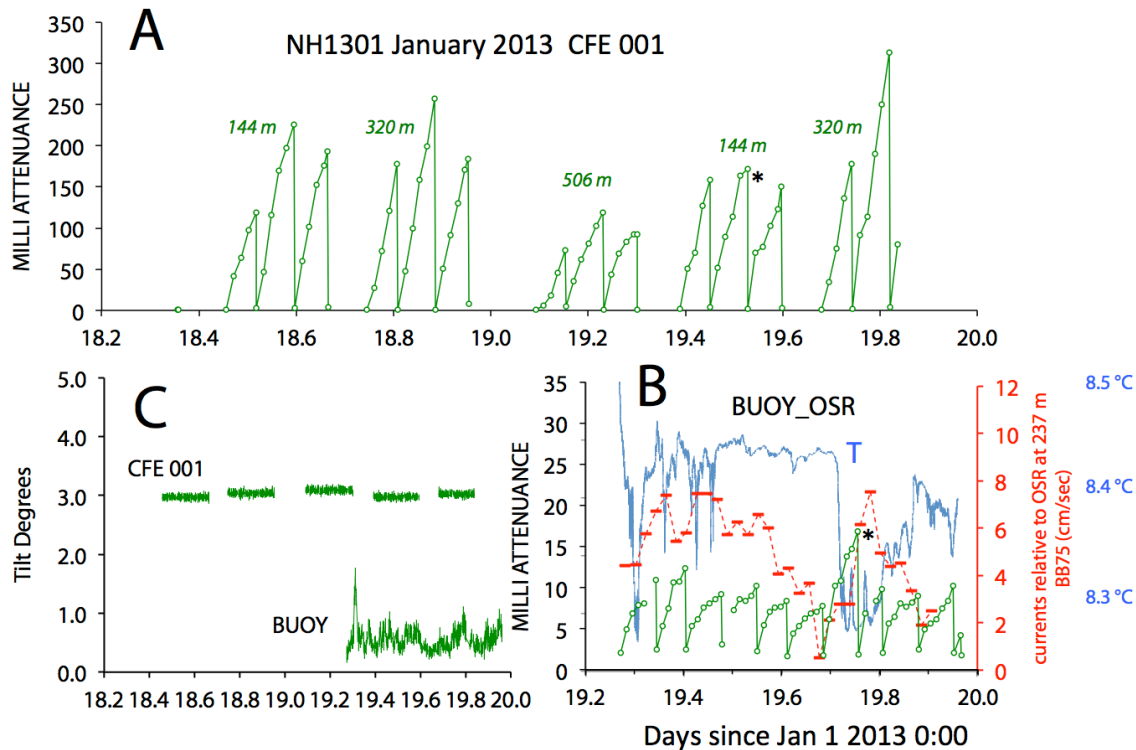


Figure 8. Time series of image attenuation from CFE and BUOY-OSR deployments in the Santa Cruz Basin during January 2013. Time axis is elapsed days since January 1 at 0000 UTC. In (A) and (B), the green lines depict the ATN time series. In (B), red symbols depict currents relative to the BUOY-OSR at a depth of 237 m that were calculated using ship broad band acoustic current profiler data (RDI Instruments, Ocean Surveyor 75; methods described by Hummon and Firing (2003) and 30 minute BUOY-OSR GPS positions. The current dropped briefly below  $1 \text{ cm s}^{-1}$  and the rate of accumulation of particles in the BUOY-OSR increased. This moment was also the time when the first large aggregates were seen. Also shown in (B) in blue is the temperature time series from the logging CTD. The most obvious effect on particle collection rate by the BUOY-OSR was the relative lull in currents near day 19.68. Images from samples depicted by \* are compared in Figure 9. (C) Time series of CFE and BUOY-OSR tilt in degrees. CFE tilt averaged 3 degrees, whereas BUOY-OSR tilt averaged 0.5 degrees.

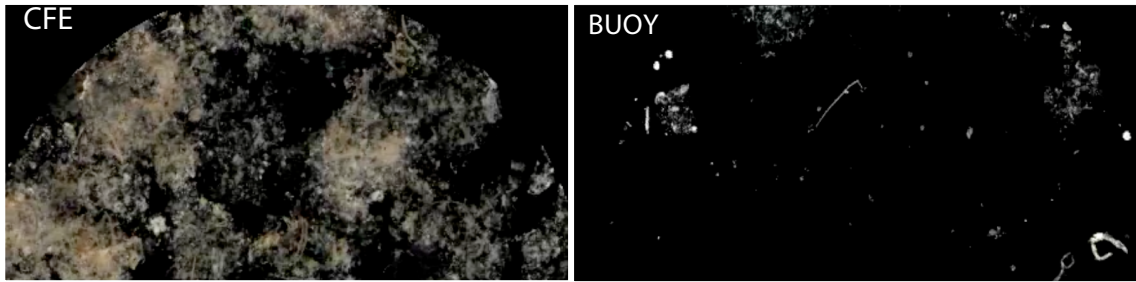


Figure 9. Comparison of representative Dark Field Images of accumulated settling particles over a 2.5 hour period from an Optical Sedimentation Recorder (OSR) on the Carbon Flux Explorer (CFE, upper left) vs. that from a surface BUOY-tethered OSR (upper right) during NH1301 (Jan. 2013). The CFE was observing sedimentation at 320 m (image 21:14 UTC). The BUOY-OSR was deployed at 237 m (image 18:07 UTC). Each image is 2.5 cm across and pixel resolution is 14  $\mu\text{m}$ . The Large fluffy 0.5 – 1.0 cm sized marine snow aggregates were almost completely missed by the BUOY OSR. Winds were near calm ( $< 5 \text{ m s}^{-1}$ ) and surface waves and swell were almost entirely absent. The BUOY system had  $\sim 0.5^\circ$  of tilt. The only difference between the CFE and BUOY was the absence/presence of tidally fluctuating horizontal currents of up to  $8 \text{ cm sec}^{-1}$ . Only fragments of the marine snow particles were seen in the BUOY samples.

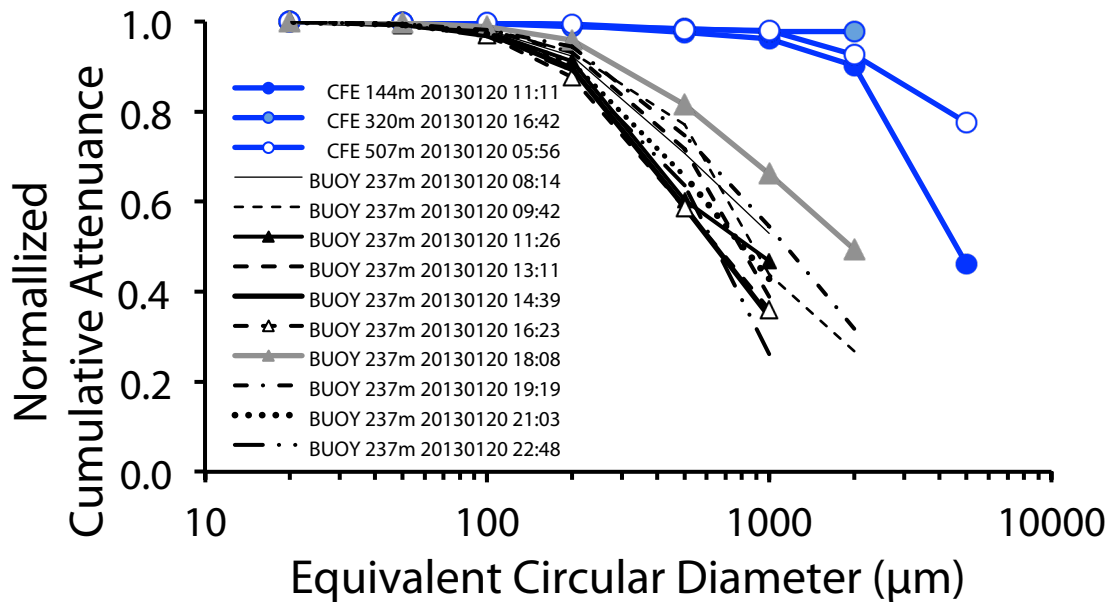


Figure 10. Comparison of Normalized Cumulative Attenuance – Size Distribution for images from CFE and BUOY-OSR systems, January 2013. Over 96% of the cumulative volume attenuation loading was in the >1000 μm fraction in CE samples. The BUOY system images at 11:26 and 18:08 corresponded to times when current velocity above the mouth of the trap was 6 cm s<sup>-1</sup> and less than 2 cm s<sup>-1</sup>, respectively. The cumulative distributions for the BUOY-OSR can be matched by eliminating all of the >1500 μm sized material from the CFE size distributions.

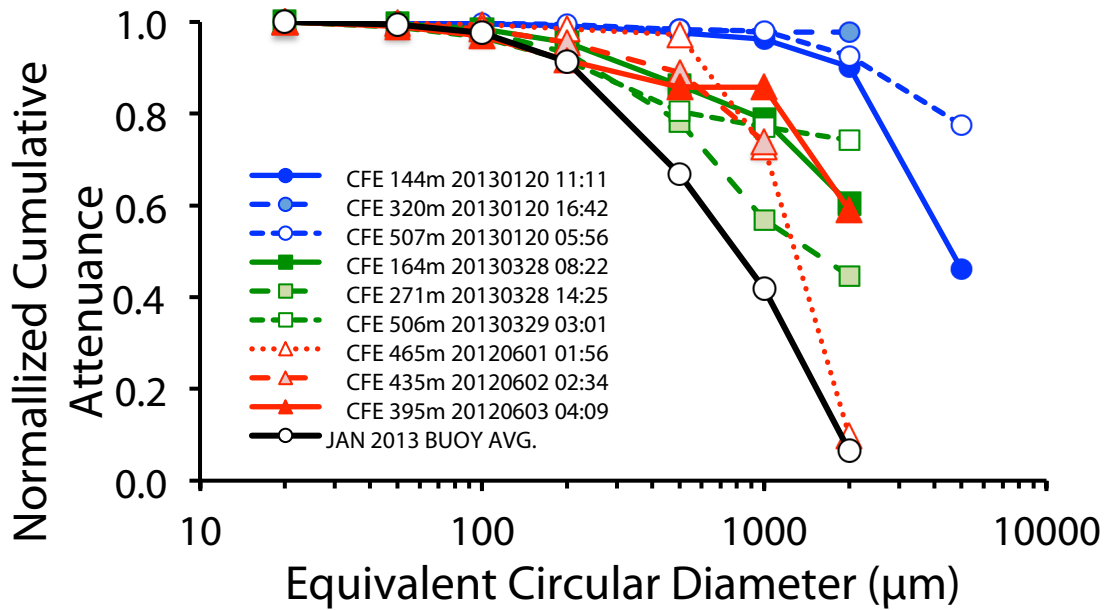


Figure 11. Comparison of Normalized Cumulative Volume Attenuance – Size Distributions (CVA-SD) from CFE deployments in May 2012 (red lines and symbols), January 2013 (blue), and March 2013 (green). Shown in black is the average CVA-SD from BUOY-OSR deployments. No CFE data from any of the three expeditions overlapped BUOY-OSR results from January 2013; in all cases, larger particles were observed by the CFE.

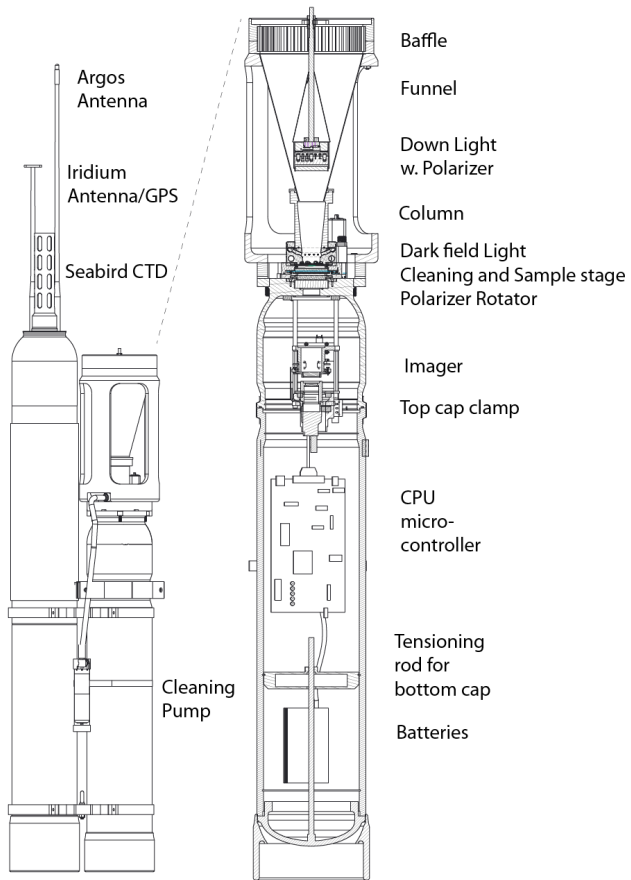


Figure A1. Drawing depicting the configuration of CFE001 and detail of lighting/imaging elements of the Optical Sedimentation Recorder (OSR). During operation, the OSR uses a 3 axis accelerometer to monitor system tilt.

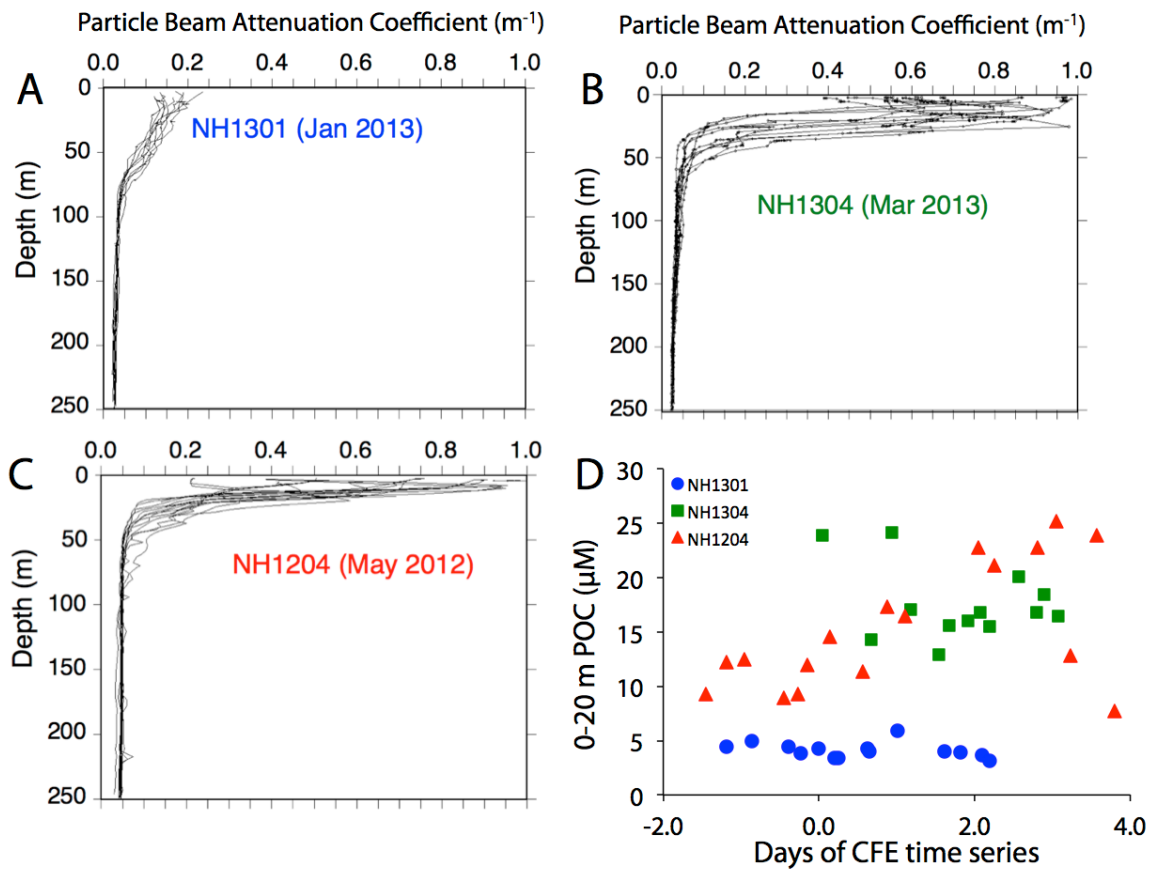


Figure A2. (A-C) Particle beam attenuation coefficient ( $c_p$ ) profiles corresponding to NH1301 (Jan 2013), NH1304 (Mar. 2013), and NH1204 (May/June 2012) Expeditions. (D) POC calculated for the 0-20 m depth interval using  $c_p$  multiplied by 27. The x axis is in days relative to the start of each CFE deployment.

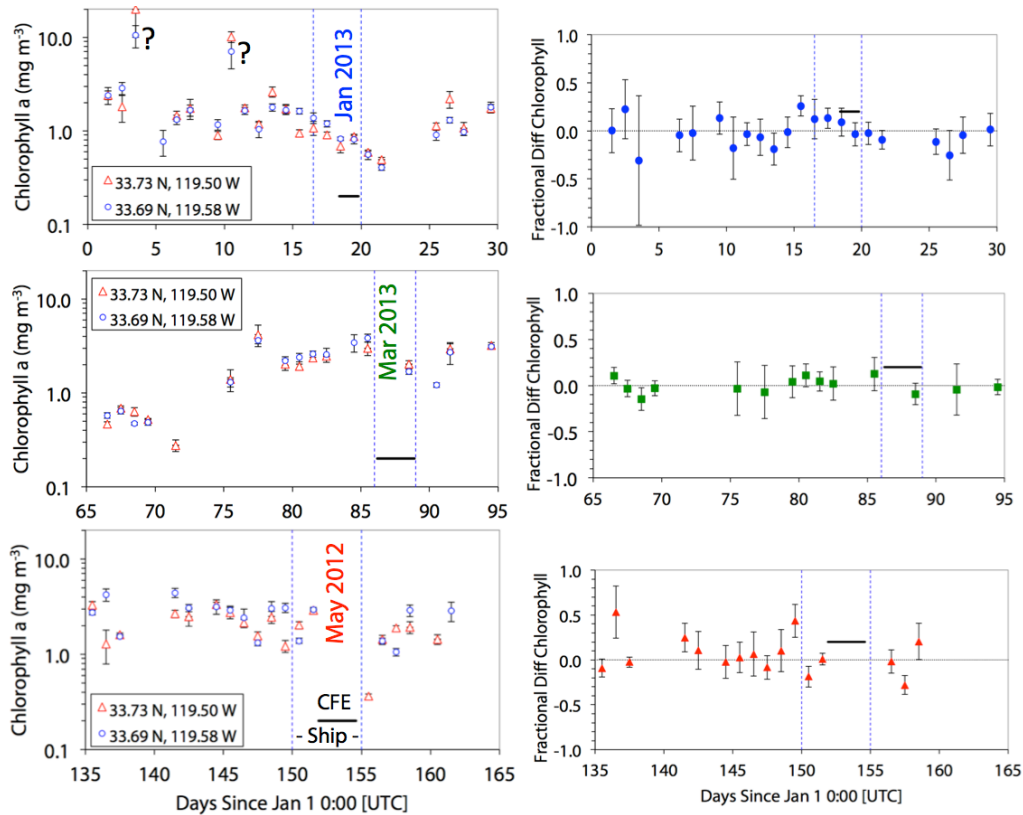


Figure A3. Left Panels: Means and standard deviations of chlorophyll a retrieved from 1 km spatially resolved merged MODIS Aqua/Terra and VIIRS Sumoi products within 2 km radius of 33.73N, 119.50W (red triangles) and 33.69N, 119.58W (blue circles). Top to bottom graphs correspond to times of sampling. Dashed blue lines denote the periods that the ship was on station in the Santa Cruz Basin study area. The black horizontal line denotes duration of CFE deployments. Right panels show the fractional difference in mean chlorophyll between the two locations. There was no systematic difference between locations.

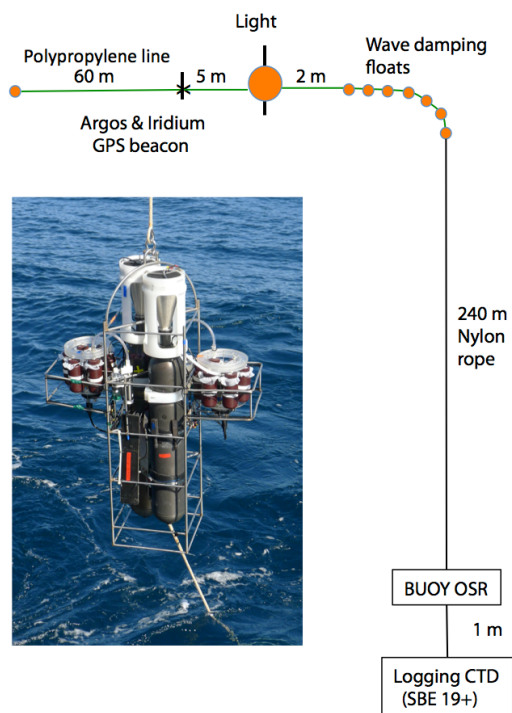


Figure A4. Photograph of the surface tethered BUOY-OSR as deployed in January 2013. Also shown is the mooring configuration used in this study. The seven small floats spaced 1 m apart are intended to minimize the effects of surface wave action on the up and down motion of the subsurface sediment trap. During the January 2013 deployment depth was 237 m ( $\pm 0.25$  m S.D.) – Maximum peak to trough vertical motion was 1 m.